

# Non-Centrosymmetric Heavy-Fermion Superconductors

N. Kimura and I. Bonalde

**Abstract** In this chapter we discuss the physical properties of a particular family of non-centrosymmetric superconductors belonging to the class heavy-fermion compounds. This group includes the ferromagnet UIr and the antiferromagnets CeRhSi<sub>3</sub>, CeIrSi<sub>3</sub>, CeCoGe<sub>3</sub>, CeIrGe<sub>3</sub> and CePt<sub>3</sub>Si, of which all but CePt<sub>3</sub>Si become superconducting only under pressure. Each of these superconductors has intriguing and interesting properties. We first analyze CePt<sub>3</sub>Si, then review CeRhSi<sub>3</sub>, CeIrSi<sub>3</sub>, CeCoGe<sub>3</sub> and CeIrGe<sub>3</sub>, which are very similar to each other in their magnetic and electrical properties, and finally discuss UIr. For each material we discuss the crystal structure, magnetic order, occurrence of superconductivity, phase diagram, characteristic parameters, superconducting properties and pairing states. We present an overview of the similarities and differences between all these six compounds at the end.

## 1 CePt<sub>3</sub>Si

The enormous interest in superconductors without inversion symmetry started with the discovery of superconductivity in the heavy-fermion compound CePt<sub>3</sub>Si [1], which exhibits long-range antiferromagnetic (AFM) order below the Neel temperature  $T_N = 2.2$  K and becomes superconducting at the critical temperature  $T_c = 0.75$  K. CePt<sub>3</sub>Si is the only known heavy-fermion (HF) compound without inversion symmetry that superconducts at ambient pressure, as opposed to the cases of CeIrSi<sub>3</sub>, CeRhSi<sub>3</sub>, CeCoGe<sub>3</sub>, CeIrGe<sub>3</sub> and UIr. The heavy-fermion character has

---

Noriaki Kimura

Center for Low Temperature Science, Tohoku University, Sendai, Miyagi 980-8578, Japan. e-mail: kimura@mail.clts.tohoku.ac.jp

Ismardo Bonalde

Centro de Física, Instituto Venezolano de Investigaciones Científicas, Apartado 20632, Caracas 1020-A, Venezuela. e-mail: ijbonalde@gmail.com

been established from the large Sommerfeld coefficient  $\gamma_n \approx 0.39 \text{ J/K}^2 \text{ mol}$  [1]. The coexistence of antiferromagnetism and superconductivity has been proved by zero-field muon-spin relaxation [2] and neutron scattering [3]. Although  $\text{CePt}_3\text{Si}$  has been intensively studied both theoretically and experimentally many questions regarding its superconducting state remain unresolved, in part because the observed properties have some sample dependence. We will focus here on the superconducting properties of  $\text{CePt}_3\text{Si}$ , giving only a brief review on normal state and magnetic behaviors (a detailed review of these can be found in Refs. [4, 5]).

### 1.1 Crystal Structure, Sample Growth and Characteristic Parameters

$\text{CePt}_3\text{Si}$  crystallizes in a tetragonal crystal structure with space group  $P4mm$  (No. 99) without inversion symmetry [1]. The lattice parameters are listed in Table 1. The unit cell has one formula unit with one Ce, one Si and two Pt inequivalent sites. The absence of inversion symmetry comes from the missing mirror plane  $(0, 0, \frac{1}{2})$  (see Fig. 1). The antiferromagnetic lattice has an ordered wave vector  $(0, 0, 1/2)$ , with a magnetic moment oriented ferromagnetically along the axis  $[100]$  and antiferromagnetically along the axis  $[001]$ , as indicated in Fig. 1.

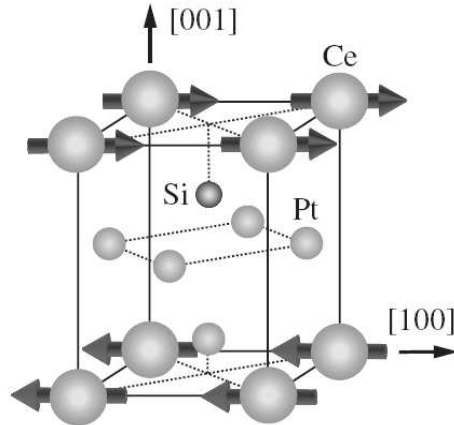


**Fig. 1** Crystal and magnetic structures of  $\text{CePt}_3\text{Si}$ .

The melting temperature of  $\text{CePt}_3\text{Si}$  is about  $1390 \text{ }^\circ\text{C}$  [6]. An isothermal section of the Ce-Pt-Si phase diagram at  $600 \text{ }^\circ\text{C}$  was presented by Griбанov et al. [6], who indicated that the interaction of Ce, Pt and Si leads to the formation of at least nine stable ternary phases. Seven of these ternary phases have a fixed composition. Polycrystalline samples of  $\text{CePt}_3\text{Si}$  have been grown by argon arc melting and high-frequency melting and single crystals by the Bridgman and high-frequency tech-

niques. These samples are usually annealed under high vacuum around 900 °C for 2-3 weeks. Interestingly, the annealing process has been linked to a Si excess [7]. Growing very high quality single crystals of CePt<sub>3</sub>Si has taken a long path that has led to the resolution of most of the problems in identifying the true superconducting properties of this compound.

**Table 1** Normal and superconducting parameters of CePt<sub>3</sub>Si

Crystal structure	tetragonal
Space group	$P4mm$
Lattice parameters	$a = 4.072 \text{ \AA}$ $c = 5.442 \text{ \AA}$
Sommerfeld value of specific heat at $T_c$	$\gamma_n = 300 - 400 \text{ mJ/mol K}^2$
Effective electron mass (Fermi sheet $\alpha$ )	$m^* \sim 11 - 23 m_0$
Mean free path	$l = 1200 - 2700 \text{ \AA}$
Antiferromagnetic transition temperature	$T_N = 2.2 \text{ K}$
Antiferromagnetic propagation vector	$\mathbf{q} = (0, 0, 1/2)$
Staggered magnetic moment $\mathbf{m}_Q$ along	[100]
Ordered moment per Ce atom	$\mu_s = 0.16 \mu_B$
Superconducting transition temperature	$T_c = 0.75 \text{ K}$ (or 0.5 K ?)
Specific heat jump at $T_c$	$\Delta C/\gamma_n T_c \approx 0.25$
Upper critical field (small anisotropy)	$H_{c2}(0) \sim 3 \text{ T}$
Thermodynamic critical field	$H_c(0) = 26 \text{ mT}$
Ginzburg-Landau coherence length	$\xi(0) \sim 104 \text{ \AA}$
Ginzburg-Landau parameter	$\kappa = 82$
London penetration depth	$\lambda(0) \approx 0.86 \mu\text{m}$
Nodal structure	Line nodes

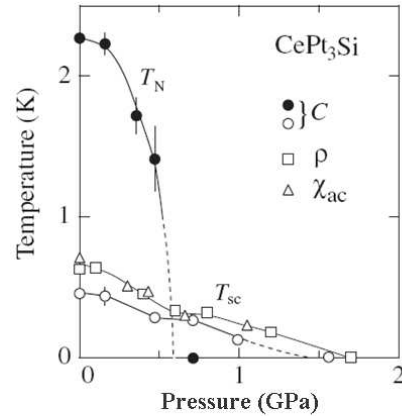
## 1.2 Normal State

### 1.2.1 Phase Diagram and Magnetic Properties

Figure 2 shows the temperature-pressure phase diagram of CePt<sub>3</sub>Si determined by specific heat, resistivity and ac magnetic susceptibility measurements [8]. The antiferromagnetic  $T_N$  and superconducting  $T_c$  transition temperatures decrease with increasing pressure and become zero around  $P_{AF} = 0.7 \text{ GPa}$  and  $P_c = 1.6 \text{ GPa}$ , respectively.

The phase diagram indicates that there are two distinct superconducting phases: one below  $P_{AF}$  coexisting with the AFM phase and another above  $P_{AF}$  being presumably the only ordered phase. The coexistence of the superconducting and AFM phases was confirmed by neutron-scattering measurements that clearly show two superlattice peaks below and above the superconducting critical temperature (see Fig. 3) [3]. The observed peaks (00 1/2) and (1 0 1/2) correspond to an AFM vec-

**Fig. 2** Temperature-pressure phase diagram of CePt<sub>3</sub>Si showing the coexistence of the antiferromagnetic and superconducting phases for pressures below 0.7 GPa [8].



for  $Q_0 = (001/2)$ . The magnetic structure consists of ferromagnetic sheets of rather small Ce moments of  $0.16 \mu_B/\text{Ce}$  stacked antiferromagnetically along the  $c$  axis (see Fig.1). Here,  $\mu_B$  is the Bohr magneton. The small value of the moment relative to  $2.54 \mu_B/\text{Ce}$  of  $\text{Ce}^{3+}$  may partially be explained through the itinerant character of Ce  $4f$ -electrons involved in the formation of the heavy quasiparticles. In parts the reduction of the moment is also due to the Kondo screening effect viewing these electrons as almost localized moments [1]. In general, the magnetic response of CePt<sub>3</sub>Si in the normal state involves also the interplay of crystal electric field splitting of the  $4f$ -orbitals and Kondo interaction (see, for example, Ref. [5]).

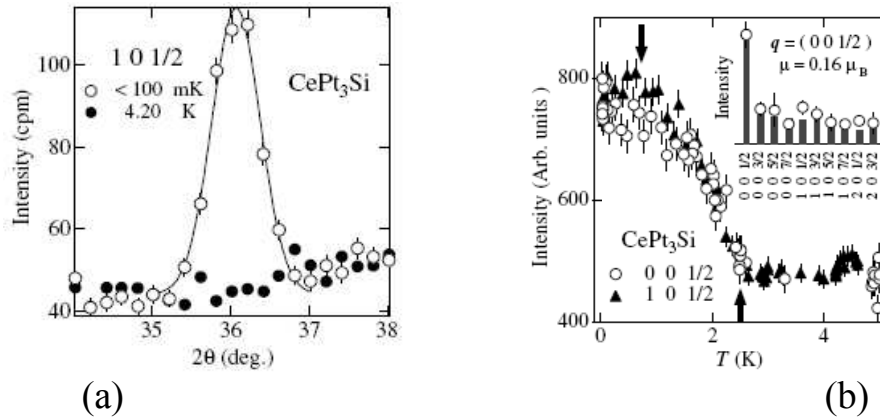


**Fig. 3** (a)  $(101/2)$  AFM Bragg reflection observed below 0.1 K (open circles) and the background measured at 4.2 K (solid circles). (b) The intensity of  $(001/2)$  and  $(101/2)$  magnetic reflections as a function of temperature, shown by open circles and solid triangles, respectively. Up and down pointing arrows indicate  $T_N$  and  $T_c$ , respectively [3].

### 1.3 Superconducting State

At ambient pressure superconductivity in CePt<sub>3</sub>Si appears within a Fermi-liquid state, as evidenced by quantum oscillations [9] and resistivity measurements [1, 10]. However, CePt<sub>3</sub>Si becomes a non-Fermi-liquid under pressure, as indicated by the linear temperature behavior of the resistivity above 0.4 GPa [10].

Most of the unusual superconducting properties found initially in CePt<sub>3</sub>Si have been clarified by now, but others have appeared. First results, like second anomalies or a small peak just below the superconducting transition in the NMR  $1/T_1T$ , are not observed in the latest measurements carried out on new single crystals. These early results were associated with sample dependence: sample preparation, off-stoichiometry, impurity phases and/or annealing conditions. The new puzzling feature is a transition temperature that falls sometimes below 0.5 K. [11, 12, 13, 14].

Several theoretical approaches have been developed to try to understand this superconductor [15, 16, 17, 18, 19]. The models take into account the splitting of the spin-degenerate bands caused by the absence of inversion symmetry. Antiferromagnetic order effects in the heavy-fermion superconductors are also considered [18, 19]. Even though much experimental and theoretical efforts have been dedicated to clarify its physics, CePt<sub>3</sub>Si continues to be the most interesting and challenging of all superconductors without spatial inversion symmetry.

#### 1.3.1 Probing the Pairing Symmetry

Several techniques have been employed to test the Cooper pairing state in non-centrosymmetric CePt<sub>3</sub>Si. We will review what has been done thus far.

#### Spin State

One of the most direct probes of the spin state of the pairing is the ratio of the superconducting to the normal electron-spin paramagnetic susceptibility,  $\chi_s$  and  $\chi_n$ , respectively, which for a spin-singlet pairing state may be written as

$$\frac{\chi_s}{\chi_n} = -2 \int_0^\infty d\xi \left\langle \frac{\partial f(E)}{\partial E} \right\rangle_{\hat{k}}. \quad (1)$$

The integration is over  $\xi$ , the energy of the free electrons relative to the Fermi level,  $f$  is the Fermi distribution function, and  $E = \sqrt{\xi^2 + \Delta(\hat{k})^2}$  is the energy of the quasiparticles. The bracket  $\langle \dots \rangle_{\hat{k}}$  denotes the angular average. Here,  $\Delta(\hat{k})$  is the energy gap that in general depends on the momentum direction  $\hat{k}$  and temperature. For  $T \ll T_c$  the ratio  $\chi_s/\chi_n$  goes as  $(1/\sqrt{T}) \exp(-\Delta_0/k_B T)$  for an  $s$ -wave pairing state with an isotropic gap and as  $T^2$  for a  $d$ -wave pairing state where the gap has

line nodes (Fig. 4(a)).  $\Delta_0$  is the zero-temperature value of  $\Delta$  and  $k_B$  is the Boltzmann constant.

For spin-triplet pairing the ratio  $\chi_s/\chi_n$  is more complicated and depends on the field orientation. In the most simple cases, the susceptibility does not change across the transition if the field is perpendicular to the  $\mathbf{d}$  vector denoting the spin-triplet gap function, but decreases continuously down to zero at  $T = 0$  if the applied field is parallel to the  $\mathbf{d}$  vector (Fig. 4(b)).

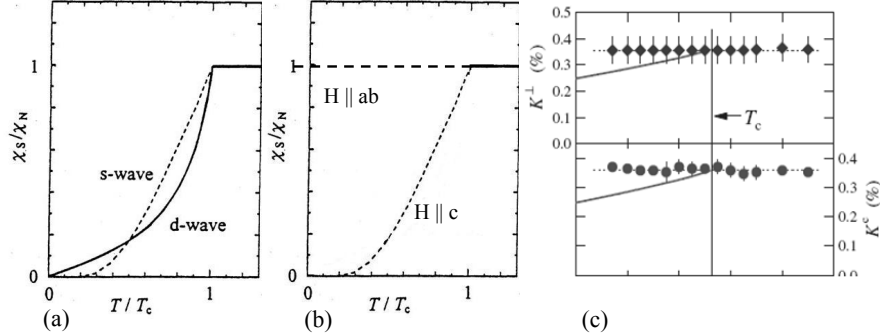


**Fig. 4** Electronic spin susceptibility expected in (a) spin-singlet states *s*-wave and *d*-wave and (b) spin-triplet states. (c) Experimental electronic spin susceptibility of CePt<sub>3</sub>Si showing no change across the superconducting transition for all orientations of the applied magnetic field (upper panel:  $\mathbf{H} \perp \hat{z}$  and lower panel  $\mathbf{H} \parallel \hat{z}$ ) [20].

In CePt<sub>3</sub>Si the experimental result of  $\chi_s/\chi_n$  is puzzling:  $\chi_s/\chi_n$  does not change at all in the superconducting phase for any orientation of the field as shown in Fig. 4(c) [20]. Model calculations including a sizable ASOC characteristic for the non-centrosymmetric CePt<sub>3</sub>Si predict that for both spin-singlet and spin-triplet states  $\chi_s(0)/\chi_n \rightarrow 1$  for fields parallel to the *z* axis and  $\chi_s(0)/\chi_n \rightarrow 1/2$  for fields perpendicular to *z* [21, 22]. On the other hand, if electron correlations are included,  $\chi_s/\chi_n$  can be calculated to be constant across the transition independently of the field orientation [18, 19]. Thus, in CePt<sub>3</sub>Si spin-susceptibility measurements are not quite useful to distinguish between spin-singlet and spin-triplet pairings.

The upper critical field  $H_{c2}$  can also be used to get information about the spin configuration of a pairing state. A magnetic field induces pair breaking via paramagnetic and orbital mechanisms. The Pauli paramagnetic limiting field  $H_P$  can be estimated by comparing the (zero-field) superconducting condensation energy with the Zeeman energy

$$\frac{1}{2}(\chi_n - \chi_s)H_P^2 = \frac{1}{2}N_0\Delta_0^2, \quad (2)$$

where  $N_0$  is the density of states at the Fermi energy. The Pauli susceptibility  $\chi_n$  is given by  $\chi_n = (g\mu_B)^2 N_0/2$ , where  $g$  is the gyromagnetic ratio.  $H_P$  is then derived as

$$H_P = \frac{\sqrt{2}\Delta_0}{g\mu_B\sqrt{1-\chi_s/\chi_n}}. \quad (3)$$

As discussed above, for spin-singlet superconductors  $\chi_s$  goes to zero as  $T \rightarrow 0$ . Then, using the BCS value  $\Delta_0 = 1.76k_B T_c$  for a weak-coupling superconductor and  $g = 2$  for free electrons, we obtain the well-known estimate

$$H_P^{BCS} = H_P(0) = 1.86T_c [\text{T/K}]. \quad (4)$$

This expression is also valid for spin-triplet superconductors if the field is applied parallel to the  $\mathbf{d}$  vector. On the other hand, if the field is applied perpendicular to the  $\mathbf{d}$  vector  $\chi_s = \chi_n$  as  $T \rightarrow 0$  and Eq. (3) yields  $H_P \rightarrow \infty$ . This would imply the absence of the Pauli paramagnetic limiting effect for fields along the  $ab$  plane.

Measurements on high-quality single crystals of  $\text{CePt}_3\text{Si}$  show a weak anisotropy for the upper critical field  $H_{c2}(0)$  with a value around 3 T (Fig. 5) [10] that exceeds the standard BCS weak-coupling paramagnetic limit  $H_P(0) \approx 1$  T.

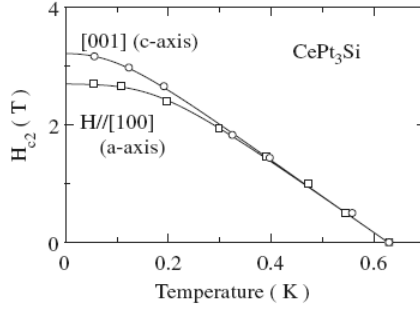


**Fig. 5** Temperature dependence of the upper critical field in  $\text{CePt}_3\text{Si}$  showing a weakly anisotropic behavior [10].

From Eq. (3) and the predictions for  $\chi_s/\chi_n$  in the non-centrosymmetric superconductors, no limiting behavior is expected for fields parallel to the  $c$  axis, whereas  $H_P(0) = \Delta_0/\mu_B \approx 1.4$  T for fields in the  $ab$  plane. As mentioned above, modifications of  $\chi_s$  due to correlation effects as well as magnetic ordering could eliminate the paramagnetic limiting for all field directions [18, 19]. It was also suggested that the realization of a so-called helical phase for fields perpendicular to the  $c$  axis would strongly reduce paramagnetic limiting effects [23, 24].

The orbital limiting field  $H_{orb}$  is expressed by

$$H_{orb}(T) = \frac{\Phi_0}{2\pi\xi^2(T)}, \quad (5)$$

where  $\Phi_0$  is the flux quantum.  $H_{orb}(T=0)$  can be in principle obtained by using the BCS expression  $\xi(0) = 0.18\hbar v_F/(k_B T_c)$ , where  $v_F$  is the Fermi velocity. However,  $H_{orb}(T=0)$  is usually estimated from the formula [25]

$$H_{orb}(T) = h(T)H'_{c2}T_c. \quad (6)$$

Here,  $H'_{c2} \equiv -dH_{c2}/dT|_{T=T_c}$ .  $h(0) = 0.727$  for weak-coupling BCS superconductors in the clean limit. Using the data of Fig. 5 we estimate  $H'_{c2} \approx -6.8$  T/K and from Eq. (6)  $H_{orb}^{BCS} \approx 3.7$  T. This is about the value of  $H_{c2}(0)$  for both field orientations, which suggests that CePt<sub>3</sub>Si may be restricted by the orbital depairing limit. In such a case the spin-triplet state should be favorable. Both paramagnetic and orbital mechanisms will be discussed in more detail in Sect. 2.

## Nodal Structure

The structure of the energy gap is directly related to the symmetry of the Cooper pairing. The energy gap is isotropic for  $s$ -wave spin-singlet superconductors and usually has zeroes (nodes) for other symmetries. Thus, the determination of the presence of nodes in the energy gap is crucial to establish pairing with symmetries lower than the  $s$ -wave. The existence of nodes in the energy gap leads to low-temperature power laws ( $T^n$ ) in several superconducting properties, instead of the BCS exponential temperature response observed for an isotropically gapped excitation spectrum. In CePt<sub>3</sub>Si magnetic penetration-depth, thermal-conductivity and specific-heat measurements show power-law behaviors indicative of line nodes in the energy gap.

A linear temperature dependence of the magnetic penetration depth  $\lambda(T)$  below  $0.16 T_c$  was first found in a polycrystalline sample of CePt<sub>3</sub>Si (Fig. 6(a)) [26], and later also in single crystals [13]. In the local limit of the electrodynamics of superconductors, the magnetic penetration depth is given by

$$\left[ \frac{\lambda^2(0)}{\lambda^2(T)} \right]_{ij} = \frac{n_{ij}^s(T)}{n} = 3 \left\langle \hat{k}_i \hat{k}_j \left[ 1 - \int d\xi \left( \frac{-\partial f}{\partial E_{\mathbf{k}}} \right) \right] \right\rangle_{\hat{k}}. \quad (7)$$

In superconductors with inversion symmetry  $\Delta\lambda(T) \propto T$  is expected in the low-temperature limit for an energy gap with line nodes [27]. Thus, the linear response in CePt<sub>3</sub>Si was taken as evidence for line nodes. Surprisingly, the temperature response in the penetration depth is not affected by the sample quality, as opposed to what occurs in unconventional superconductors with line nodes in the gap [13]. Figure 6(b) displays the low-temperature region of the penetration depth of several single crystals of different quality. A clear linear behavior is observed in all of them. We note that the superfluid density  $\rho_s(T)$  shows a small anisotropy [28], in agreement with the upper critical field result.

Thermal transport measurements also suggest the presence of line nodes by showing a residual linear term in  $\kappa(T)/T$  as  $T \rightarrow 0$  (Fig. 7(a)). In superconductors with inversion symmetry such a linear term is expected when the energy gap has nodes, and is due to impurity scattering. The quasiparticle thermal conductivity has universal components in the low-temperature limit ( $k_B T < \gamma$ )

$$\kappa_{ii} = \frac{\pi^2}{3} N_0 v_F^2 T \left\langle \hat{k}_i \hat{k}_i \frac{\gamma^2}{(\gamma^2 + \Delta_{\mathbf{k}}^2)^{3/2}} \right\rangle_{\hat{k}} \quad (8)$$



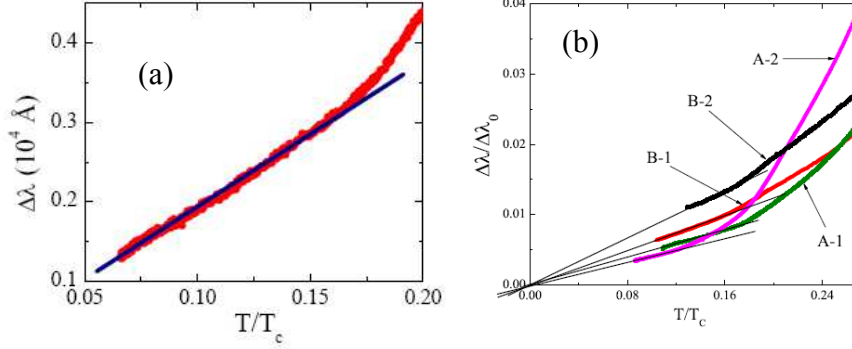


**Fig. 6** Penetration depth in (a) a polycrystalline sample and (b) single crystals of CePt<sub>3</sub>Si. The linear temperature behavior indicates line nodes in the energy gap. The single crystals used in the penetration-depth measurements shown in (b) have different defect concentrations, which suggests that the linear behavior is unaffected by disorder [13].

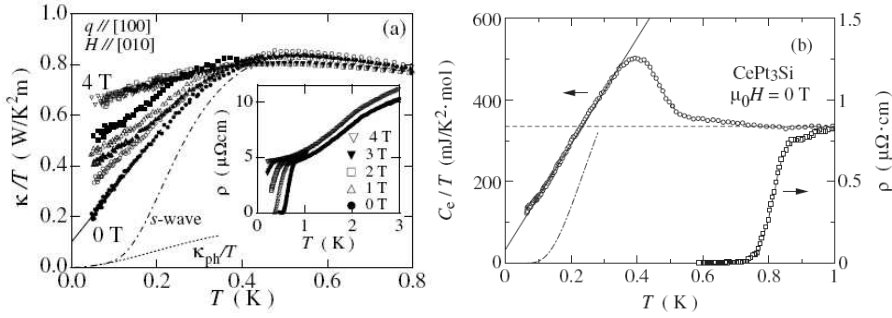


**Fig. 7** Temperature dependence of (a) thermal conductivity [29] and (b) specific heat [30] of CePt<sub>3</sub>Si. The linear temperature response suggests line nodes in the energy gap.

that are linear functions of temperature at low  $T$  and whose proportionality constants depend on the specific form of the order parameter [27].  $\gamma$  is the quasiparticle decay rate. In CePt<sub>3</sub>Si the experimental  $\kappa(T)/T = 0.1 \text{ W}/(\text{K}^2 \cdot \text{m})$  is in good agreement with the calculated universal conductivity limit  $0.09 \text{ W}/(\text{K}^2 \cdot \text{m})$  [29]. Moreover, the  $H$  dependence of  $\kappa$  follows the prediction by a theory of Doppler-shifted quasiparticles in a superconductor with line nodes [29, 31].

In the low-temperature limit the electronic specific heat of CePt<sub>3</sub>Si has been found to follow the expression  $C_{el}/T = A + BT$ , with  $A = 34.1 \text{ mJ}/(\text{K}^2 \cdot \text{mol})$  and  $B = 1290 \text{ mJ}/(\text{K}^3 \cdot \text{mol})$  (Fig. 7(b)) [30]. In general, the electronic specific heat is given by [27]

$$C_{el} = 2N_0 \int_{-\infty}^{\infty} d\xi \left\langle E_{\mathbf{k}} \frac{\partial f}{\partial E_{\mathbf{k}}} \right\rangle_{\hat{\mathbf{k}}} \quad (9)$$

For superconductors with inversion symmetry, in the low-temperature limit  $C_{el} \propto T^2$  for a gap with line nodes. The residual linear term in  $C_{el}/T$  of CePt<sub>3</sub>Si is considered to be caused by impurities or by electrons on part of the Fermi surface that do

not participate in superconducting. Thus, the observed behavior of the electronic specific heat is taken as evidence for line nodes in the energy gap [30].

For a theoretical discussion on line nodes in non-centrosymmetric superconductors, see other chapters in this book.

## 2 CeTX<sub>3</sub> Compounds

### 2.1 Crystal Structure and Related Compounds

Most CeTX<sub>3</sub> compounds crystallize in the BaNiSn<sub>3</sub>-type tetragonal structure with space group *I4mm* (No.107) [32]. The BaNiSn<sub>3</sub>-type structure derives from the BaAl<sub>4</sub>-type structure whose basic frame is the body-centered tetragonal lattice shown at the top in Fig. 8. There are two other derivatives of the BaAl<sub>4</sub>-type structure, the ThCr<sub>2</sub>Si<sub>2</sub> and CaBe<sub>2</sub>Ge<sub>2</sub> types. Some heavy-fermion superconductors crystallize into the former structure: e.g. CeCu<sub>2</sub>Si<sub>2</sub> [33], CeCu<sub>2</sub>Ge<sub>2</sub> [34], CePd<sub>2</sub>Si<sub>2</sub> [35], CeRh<sub>2</sub>Si<sub>2</sub> [36] and URu<sub>2</sub>Si<sub>2</sub> [37]. The latter structure is often found in *R*Pt<sub>2</sub>X<sub>2</sub> compounds [38], where *R* denotes a rare-earth element. The ThCr<sub>2</sub>Si<sub>2</sub>- and CaBe<sub>2</sub>Ge<sub>2</sub>-type structures have an inversion center, while the BaNiSn<sub>3</sub>-type structure does not. Fig. 8 displays the BaAl<sub>4</sub>-type crystal lattice and its three derivatives.

The atomic framework of the BaNiSn<sub>3</sub>-type structure can be alternatively displayed as a sequence of planes of the same atoms *R* – *T* – *X*(1) – *X*(2) – *R* – *T* – *X*(1) – *X*(2) – *R* along the *c* axis of the tetragonal structure, where *T* and *X* denote a transition metal and Si/Ge, respectively. The point group of the BaNiSn<sub>3</sub>-type structure is C<sub>4v</sub>, which lacks the mirror plane and a two-fold axis normal to the *c* axis (*z* axis). Therefore, a Rashba-like spin-orbit coupling exists in this system, as it does in CePt<sub>3</sub>Si that also belongs to C<sub>4v</sub> [1].

Of the CeTX<sub>3</sub> compounds, the series Ce*T*Si<sub>3</sub> (*T*=Co, Ru, Rh, Pd, Os, Ir and Pt) and Ce*T*Ge<sub>3</sub> (*T*=Fe, Co, Rh and Ir) are known to crystallize in the BaNiSn<sub>3</sub>-type structure. Among these, CeRhSi<sub>3</sub> [39], CeIrSi<sub>3</sub> [40], CeCoGe<sub>3</sub> [41] and CeIrGe<sub>3</sub> [42] have been found to be pressure-induced superconductors. Single crystals of CeRhSi<sub>3</sub> and CeIrSi<sub>3</sub>, as well as of CeRuSi<sub>3</sub> [43], can be obtained by the Czochralski pulling method in a tetra-arc furnace using a pulling speed of 10 mm/h or 15 mm/h. In these compounds annealing treatments at 900 °C, in vacuum, for a week are usually very effective. Notably, for CeRhSi<sub>3</sub> the use of stoichiometric amounts of the components sometimes yields a different crystal; e.g., CeRhSi<sub>2</sub>. To obtain a crystal of CeRhSi<sub>3</sub> an off-stoichiometric composition, typically Ce:Rh:Si=1:1:3.3, works better. Single crystals of CeCoGe<sub>3</sub> are obtained by the Bi-flux method (the Czochralski method is unsuitable) [44]. In this procedure, arc-melt-prepared ingots of CeCoGe<sub>3</sub> and Bi are placed in an alumina crucible and heated up to 1050 °C in an argon atmosphere. After keeping this temperature for a day, the crucible is cooled down to 650 °C over a period of two weeks and then down to room temperature

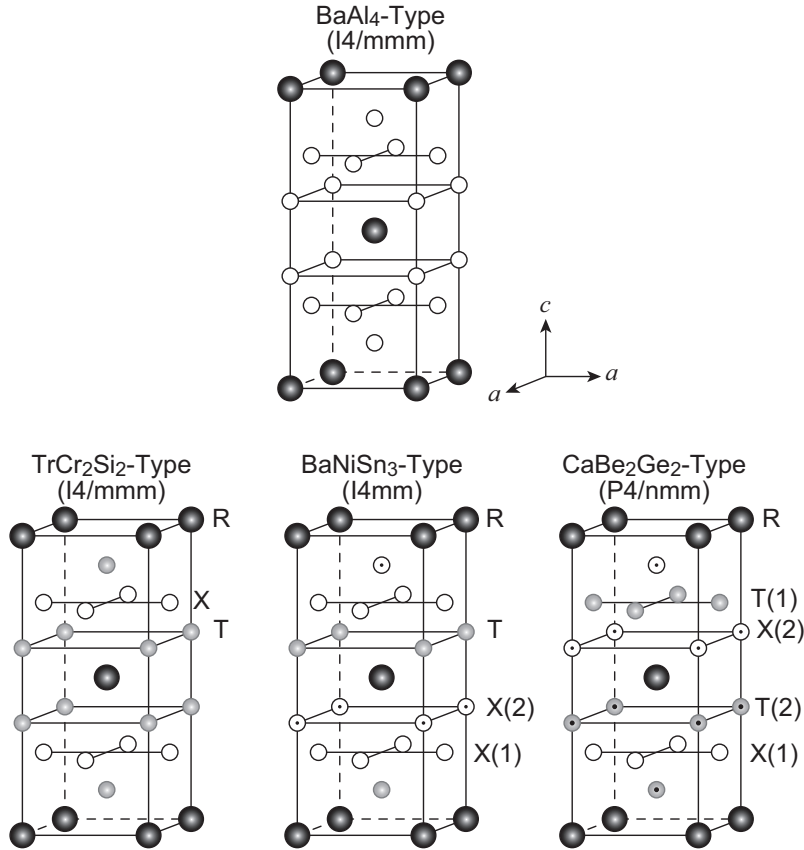


**Fig. 8**  $\text{BaAl}_4$ -type crystal structure and its three derivatives  $\text{TrCr}_2\text{Si}_2$ ,  $\text{BaNiSn}_3$  and  $\text{CaBe}_2\text{Ge}_2$ . Only the  $\text{BaNiSn}_3$ -type structure does not have an inversion center.

rapidly. Single crystals of  $\text{CeRhGe}_3$  can also be obtained by the Bi-flux technique [43]. Single crystals of  $\text{CeIrGe}_3$  are grown by the Bi- and Sn-flux methods [42, 43].

Other  $\text{CeTX}_3$  compounds with  $\text{BaNiSn}_3$ -type structure are  $\text{CeTAl}_3$  ( $T=\text{Cu, Au}$ ) and  $\text{CeAuGa}_3$ . They order magnetically at low temperatures [45, 46, 47, 48, 49]. In particular,  $\text{CeCuAl}_3$  and  $\text{CeAuAl}_3$  are suggested to be HF compounds with AFM ground states [46] and have the potential to become non-centrosymmetric HF superconductors. There are at least two  $\text{CeTX}_3$  compounds that do not have the  $\text{BaNiSn}_3$ -type crystal lattice:  $\text{CeNiGe}_3$ , which has an orthorhombic structure and exhibits superconductivity under pressure [50], and  $\text{CeRuGe}_3$ , which is reported to have either orthorhombic [51] or cubic structure [52].

On the other hand, no uranium-based compound ( $\text{UTX}_3$ ) has been fully confirmed to have the  $\text{BaNiSn}_3$ -type structure. Only  $\text{UNiGa}_3$ , that exhibits AFM order at 39 K, seems to have this structure [53].

Last, we briefly comment on non-heavy-fermion  $\text{LaTX}_3$  compounds. Some of them, like  $\text{LaRhSi}_3$ ,  $\text{LaIrSi}_3$  and  $\text{LaPdSi}_3$ , also have  $\text{BaNiSn}_3$ -type structures and show superconductivity at the critical temperature 1.9, 0.9 and 2.6 K, respectively [32, 54, 55]. In these materials, however, no evidence for unconventional behavior has been observed [54].

## 2.2 Normal State

### 2.2.1 Magnetic Properties

The  $\text{CeTX}_3$  compounds exhibit various magnetic ground states as summarized in Table 2. The magnetic ground states vary from AFM to intermediate valence (IV) through HF states with decreasing unit-cell volume  $V$ . For example,  $\text{CeCoGe}_3$  ( $V = 183.3 \text{ \AA}^3$ ) displays an AFM ground state [44, 56, 57], while  $\text{CeCoSi}_3$  ( $V = 163.6 \text{ \AA}^3$ ) is thought to be an IV compound [58].

Figure 9 shows the Néel temperature  $T_N$  and the electronic specific-heat coefficient  $\gamma_n$  as a function of unit-cell volume for  $\text{CeTX}_3$  in which  $T$  belongs to the Group 9 (Co, Rh and Ir) in the Periodic Table [43].  $T_N$  approximately follows a simple curve which peaks at  $186 \text{ \AA}^3$ . This behavior supports the Doniach model in which the on-site Kondo effect dominates over the inter-site RKKY interaction with the coupling constant  $J$  being effectively enhanced relative to the kinetic energy with decreasing unit-cell volume [43].  $\gamma_n$  is also described by a simple curve which peaks at the unit-cell volume  $176 \text{ \AA}^3$  at which  $T_N$  goes to zero, suggesting that the  $\gamma_n$  value is enhanced by the magnetic fluctuation arising at the corresponding volume.

Besides the Group 9 (Co, Rh, Ir) compounds, one can consider  $\text{CeFeGe}_3$  to be a potential superconductor because its  $\gamma_n$  is comparable to those of  $\text{CeRhSi}_3$  and  $\text{CeIrSi}_3$ . However, in  $\text{CeFeGe}_3$  superconductivity has not been observed down to 0.05 K [65].

#### **CeRhSi<sub>3</sub>**

As shown in Figs. 10(a) and 11(d), the magnetic properties of  $\text{CeRhSi}_3$  are anisotropic especially at low temperatures [55, 67]. The induced magnetization along the easy axis [100] has a quite small value of  $0.1\mu_B$  at 7 T. The magnetic susceptibility curves for  $H$  parallel to the  $a$  and  $c$  axes show a strong anisotropy at low temperatures, while they obey the Curie-Weiss law above about 150 K. The effective moments  $\mu_{eff}$  for both field directions are  $2.65\mu_B$ , which is close to the expected value for the  $\text{Ce}^{3+}$  ion. The Weiss temperatures are negative and very large ( $-112$  and  $-160$  K for  $H$  parallel to the  $a$  and  $c$  axes, respectively), as often found for IV compounds. The susceptibility for  $H \parallel c$  has a broad peak around 50 K that is characteristic of HF compounds.

From the jump of the specific heat at  $T_N$ , the magnetic entropy gain is estimated to be only 12% of  $R\ln 2$  [60]. The AFM state is robust against a magnetic field (Fig. 12(a)) and survives up to 8 T, although such a strong field should be sufficient

**Table 2** Unit-cell volume ( $V$ ), magnetic ground state, electronic specific-heat coefficient  $\gamma_n$ , ordering temperature ( $T_N$ ), Weiss temperature ( $\Theta_p$ ) and effective moment ( $\mu_{eff}$ ) for the BaNiSn<sub>3</sub>-type CeT $X_3$  compounds. The abbreviations PM and AFM denote paramagnetic and antiferromagnetic ground states, respectively. The abbreviations IV and HF denote intermediate-valence and heavy-fermion states, respectively. We consider compounds with  $\gamma_n > 100$  mJ/mol·K<sup>2</sup> to be heavy-fermion systems.

Compound	$a$ [Å]	$c$ [Å]	$V$ [Å <sup>3</sup> ]	Magnetism	$\gamma_n$ [mJ/mol·K <sup>2</sup> ]	$T_N$ [K]	$\Theta_p$ [K]	$\mu_{eff}$ [ $\mu_B$ ]	Ref.
*CeT $Si_3$									
CeCoSi <sub>3</sub>	4.135	9.567	163.6	PM(IV)	37	-	-840	2.80	[59]
CeRuSi <sub>3</sub>	4.21577	9.9271	176.43	PM(IV)		-			[43]
CeRhSi <sub>3</sub>	4.269	9.738	177.5	AFM(HF)	110	1.6	-128	2.65	[60, 55]
	4.237	9.785	175.7						[61]
CePdSi <sub>3</sub>	4.33	9.631	180.6	AFM	57	5.2/3	-26	2.56	[62, 55]
CeOsSi <sub>3</sub>				PM(IV)					[63]
CeIrSi <sub>3</sub>	4.252	9.715	175.6	AFM(HF)	120	5.0	-142	2.48	[60, 55]
CePtSi <sub>3</sub>	4.3215	9.6075	179.42	AFM	29	4.8/2.4			[64]
*CeT $Ge_3$									
CeFeGe <sub>3</sub>	4.332	9.955	186.8	PM(HF)	150	-	-90	2.6	[65]
	4.3371	9.9542	187.24						[66]
CeCoGe <sub>3</sub>	4.320	9.835	183.5	AFM	32	21/19	-51	2.54	[59]
	4.319	9.829	183.3			21/12/8			[44]
CeRhGe <sub>3</sub>	4.402	9.993	193.6	AFM	40	14.6/10/0.55	-28	2.53	[60]
	4.3976	10.0322	194.01			14.9/8.2			[43]
CeIrGe <sub>3</sub>	4.409	10.032	195.0	AFM	80	8.7/4.7/0.7	-21	2.39	[60]
	4.401	10.024	194.2			8.7/4.8			[43]

to suppress an AFM state with a low  $T_N$  of the order of 1 K. The temperature and height of the specific-heat peak decrease with increasing field along the easy axis ( $H \parallel a$ ). The magnetic contribution to the specific heat when the field is aligned with the hard axis ( $H \parallel c$ ) does not change even at 8 T [67]. The tiny entropy gain and the insensitivity to a magnetic field are attributed to the strong Kondo screening of the  $4f$  electron. The Kondo temperature is estimated to be about 50 K [60].

The magnetic structure at ambient pressure is revealed by neutron experiments to be a longitudinal spin-density-wave (LSDW) type characterized by the propagation vectors  $Q = (\pm 0.215, 0, 0.5)$  with polarization along the  $a^*$  axis [69]. The magnetic structure is shown in Fig. 13. The staggered moment  $0.13 \mu_B$  is quite small [70]. The incommensurate LSDW structure with such a strongly suppressed moment suggests that itinerant-electron magnetism is realized in CeRhSi<sub>3</sub>. The  $4f$  electrons are expected to be strongly hybridized with the conduction electrons through the Kondo effect, leading to the formation of the SDW state caused by nesting of the Fermi surface.

It is not obvious whether this magnetic structure persists under pressure. In the pressure-dependent specific-heat curve, a shoulder-like transition is seen below  $T_N$  at a pressure of 0.55 GPa [71]. The origin of the transition is unclear at present. Con-

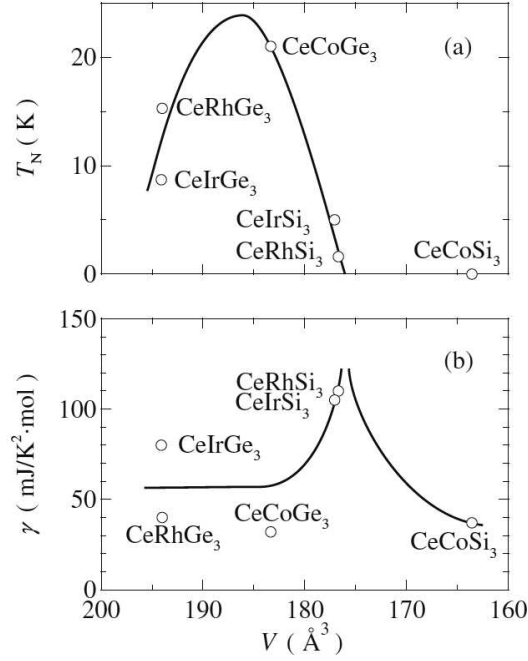


**Fig. 9** Unit-cell volume dependence of (a) the Néel temperature and (b) the  $\gamma_n$  value in  $\text{CeTSi}_3$  and  $\text{CeTGe}_3$  ( $T$ : Co, Rh, Ir) [43].

Considering that multiple magnetic transitions are observed in other magnetic  $\text{CeTX}_3$  compounds, the magnetic structure realized in  $\text{CeRhSi}_3$  at ambient pressure may change under pressure where superconductivity appears.

The electrical resistivity below  $T_N$  can be fitted by an antiferro-magnon model [72]. At sufficiently low temperatures ( $T < 0.6$  K), the resistivity follows the Fermi-liquid description of  $\rho(T) = \rho_0 + AT^2$ , where  $\rho_0$  is the residual resistivity.  $A = 0.19 \mu\Omega \cdot \text{cm}/\text{K}^2$  for the current  $J$  along the  $a$  axis and  $A = 0.24 \mu\Omega \cdot \text{cm}/\text{K}^2$  for  $J \parallel c$ . The ratios  $A/\gamma_n^2 = 1.6 \times 10^{-5}$  ( $J \parallel a$ ),  $2.0 \times 10^{-5}$  ( $J \parallel c$ )  $\mu\Omega \cdot \text{cm} \cdot \text{K}^2 \cdot \text{mol} \cdot \text{mJ}^{-2}$  are close to  $1 \times 10^{-5} \mu\Omega \cdot \text{cm} \cdot \text{K}^2 \cdot \text{mol} \cdot \text{mJ}^{-2}$  as given by the Kadowaki-Woods relation [73].

### **CeIrSi<sub>3</sub>**

Although the magnetic structure of  $\text{CeIrSi}_3$  is unknown at present, the specific heat, magnetic susceptibility and electrical resistivity are similar to those of  $\text{CeRhSi}_3$ . The magnetization curve is anisotropic and  $a$  is the easy axis (Fig. 10(b)) [68]. The magnetization increases almost linearly with magnetic field. Neither a saturation behavior nor metamagnetic transitions are observed for fields in the basal plane up to 50 T. The induced magnetization is very small and comparable to that of  $\text{CeRhSi}_3$ ;  $0.1\mu_B$  at 10 T for the easy axis. The temperature dependence of the magnetic susceptibility is anisotropic at low temperatures (Fig. 11(g)) [40, 68].

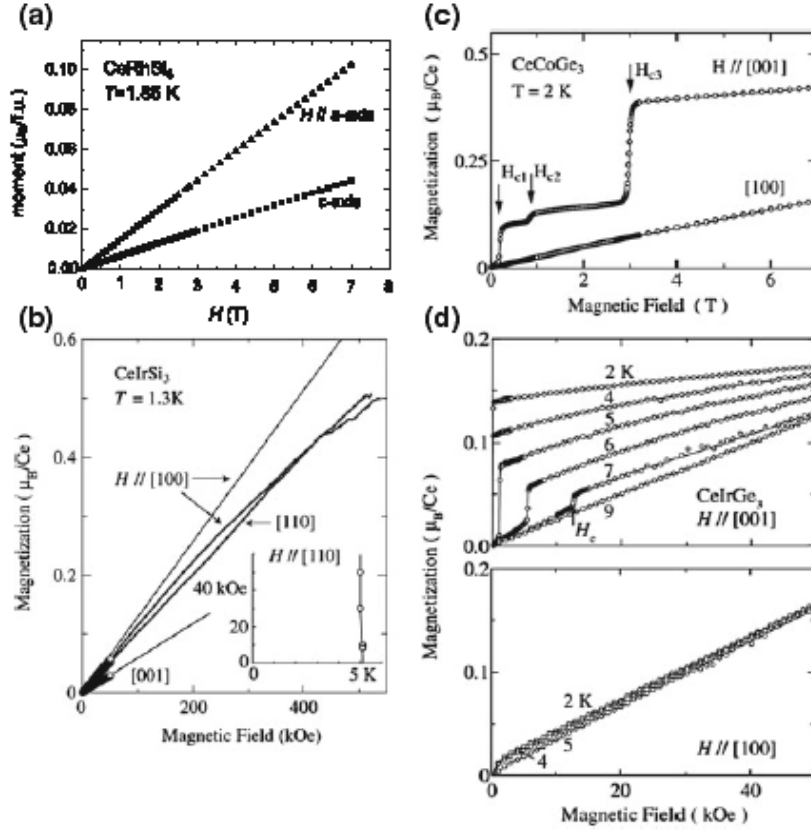
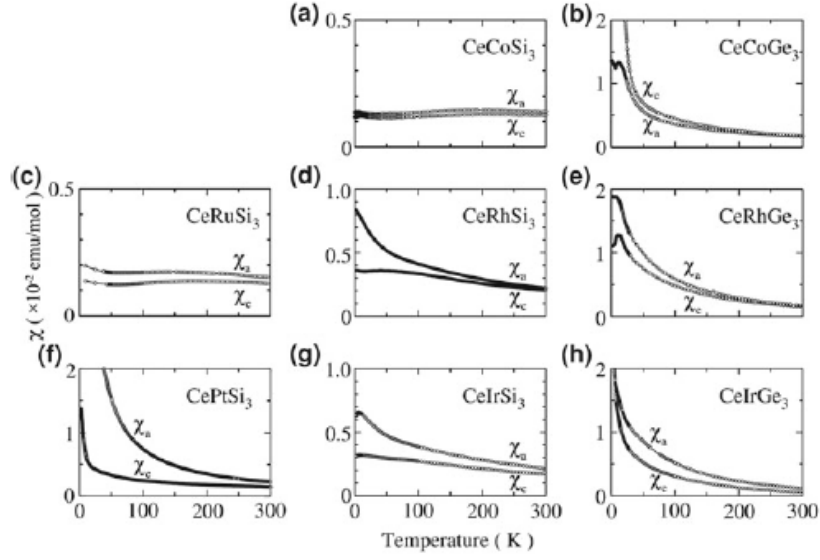


Fig. 10 Magnetization curves of CeRhSi<sub>3</sub>, CeIrSi<sub>3</sub>, CeCoGe<sub>3</sub>, and CeIrGe<sub>3</sub> [44, 55, 68].

The entropy gain associated with the AFM transition is small,  $0.2R\ln 2$ , as in CeRhSi<sub>3</sub> (Fig. 12(b)) [68]. The AFM state is robust against a magnetic field, as shown in the inset of Fig. 10(b). The electrical resistivity below  $T_N$  can be fitted by an antiferro-magnon model as done in CeRhSi<sub>3</sub>. The coefficient of the  $T^2$  term  $A = 0.04 \mu\Omega\cdot\text{cm}/\text{K}^2$  for  $J \parallel c$  and  $J \perp c$  [68] is about one fifth of the coefficients of CeRhSi<sub>3</sub>. The ratio  $A/\gamma_n^2 = 3.6 \times 10^{-6} \mu\Omega\cdot\text{cm}\cdot\text{K}^2\cdot\text{mol}\cdot\text{mJ}^{-2}$  is much smaller than the ratios in CeRhSi<sub>3</sub> but still in the range of the Kawakami-Woods relation.

### CeCoGe<sub>3</sub>

Unlike CeRhSi<sub>3</sub> and CeIrSi<sub>3</sub>, CeCoGe<sub>3</sub> exhibits three successive AFM transitions [44]. Correspondingly, the magnetization for  $H \parallel c$  shows three-step metamagnetic transitions. It reaches  $M_s/4$ ,  $M_s/3$  and  $M_s$ , where  $M_s = 0.43\mu_B/\text{Ce}$ , at each transition. The anisotropic magnetization curve indicates an Ising-like magnetism with the easy axis along the  $c$  axis, which is different from what is found in CeRhSi<sub>3</sub> and CeIrSi<sub>3</sub> as seen in Fig. 11.



**Fig. 11** Magnetic susceptibility of  $CeTX_3$  compounds as a function of temperature [43].

The neutron-diffraction experiments revealed that the magnetic structure of the ground state at ambient pressure consists of two components with dominant  $q_1=(0,0,1/2)$  and subordinate  $q_2=(0,0,3/4)$  [74]. Figure 14 shows a possible magnetic structure of the  $q_1$  sublattice. The magnetic moments are parallel to the  $c$  axis and alternate in the up-up-down-down sequence. The magnitude of the magnetic moment in the sublattice  $\mu_1$  is estimated to be  $0.5(1)\mu_B$ . A more complete magnetic structure that includes the  $q_2$  sublattice is not clear at present.

The magnetic susceptibility of  $CeCoGe_3$  does not show a peak or a saturated behavior at low temperatures as observed in  $CeRhSi_3$  and  $CeIrSi_3$ . Specific heat measurements revealed that the entropy gain reaches 68% of  $R\ln 2$  at  $T_{N1} = 21$  K and that 32% of entropy loss is recovered at 38 K. The magnetism of  $CeCoGe_3$  is basically understood in terms of localized  $4f$  electron.

### **CeIrGe<sub>3</sub>**

The magnetic structure of  $CeIrGe_3$  seems to be more complicated. There are two successive magnetic transitions at  $T_{N1}=8.7$  K and  $T_{N2}=4.8$  K. The former is anti-ferromagnetic and the latter is unknown although magnetization measurements indicate weak ferromagnetism with a small moment below  $T_{N2}$  (see Fig. 10(d)). A parasitic ferromagnetism due to the Dzyaloshinsky-Moriya interaction caused by the broken space inversion symmetry is discussed in Ref. [43].  $T_{N2}$  merges into  $T_{N1}$  with the application of pressure (see Fig. 15(d)).



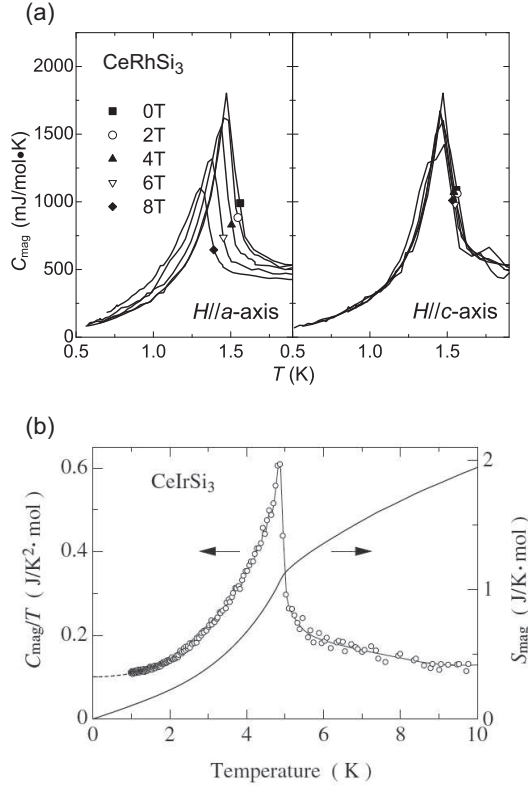
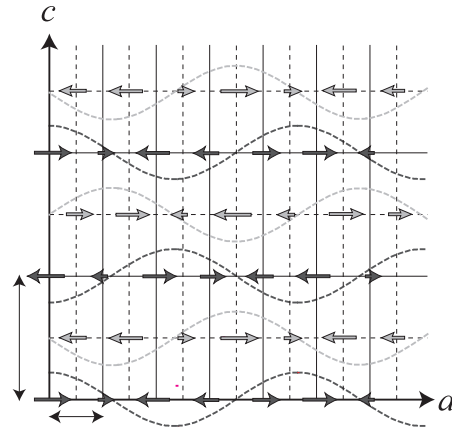


**Fig. 12** (a) Magnetic contribution to the specific heat  $C_{\text{mag}}$  of CeRhSi<sub>3</sub> as a function of temperature for fields along the  $a$  and  $c$  axes [67]. (b)  $C_{\text{mag}}/T$  and the entropy  $S$  of CeIrSi<sub>3</sub> as a function of temperature [68].

## 2.2.2 Temperature-Pressure Phase Diagram

All known  $\text{CeTX}_3$  superconductors need pressure to become superconducting. The temperature-pressure ( $T$ - $P$ ) phase diagrams of CeRhSi<sub>3</sub> [72], CeIrSi<sub>3</sub> [75], CeCoGe<sub>3</sub> [76] and CeIrGe<sub>3</sub> [42] are shown in Fig. 15. In CeRhSi<sub>3</sub>, the Néel temperature  $T_N$  initially increases and subsequently decreases with applying pressure, while those of CeIrSi<sub>3</sub> decreases monotonically with pressure. The  $T_N(P)$  of CeCoGe<sub>3</sub> and CeIrGe<sub>3</sub> exhibits step-like decreases probably relevant to successive magnetic phase transitions observed at ambient pressure. The superconducting transitions of these four compounds are observed at pressures at which the AFM order still exists. We define here three characteristic pressures:  $P_1^*$  where  $T_N = T_c$ ,  $P_2^*$  where  $T_N \rightarrow 0$  and  $P_3^*$  where the superconducting transition temperature  $T_c$  reaches a maximum. The values of these pressures are summarized in Table 3.  $P_2^*$  of CeRhSi<sub>3</sub> is unclear because  $T_N$  does not decrease steeply near  $P_1^*$ .

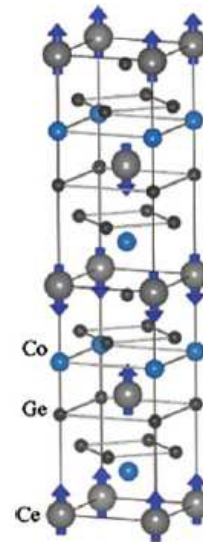
**Fig. 13** Magnetic structure of  $\text{CeRhSi}_3$ . Only the Ce sites at  $(0, 0, 0)$  and  $(0.5, 0.5, 0.5)$  positions are projected on the  $ac$  plane. The arrows are depicted to show the size and the direction of the magnetic moment at the Ce sites [70].



The resistivity drop at the superconducting transition of  $\text{CeRhSi}_3$ ,  $\text{CeIrSi}_3$  and probably  $\text{CeCoSi}_3$  has its sharpest form at  $P_3^*$ . The resistivity drop in the AFM phase, especially far below  $P_3^*$ , is very broad. In this pressure region, the drop width depends on the applied current [39, 75]. These observations imply that superconductivity is inhomogeneous or fluctuating in the antiferromagnetic state and is optimum at  $P_3^*$ . Such a phenomenon is found in centrosymmetric HF superconductors as well and, thus, seems to be realized irrespective of the presence or absence of inversion symmetry.

A similar evolution of superconductivity in the AFM state is seen by the heat capacity  $C$  (Fig. 16). The heat capacity jump ( $\Delta C$ ) at the superconducting transition

**Fig. 14** Possible magnetic structure for  $q_1=(0,0,0.5)$  sublattice in the ground state of  $\text{CeCoGe}_3$  [74].



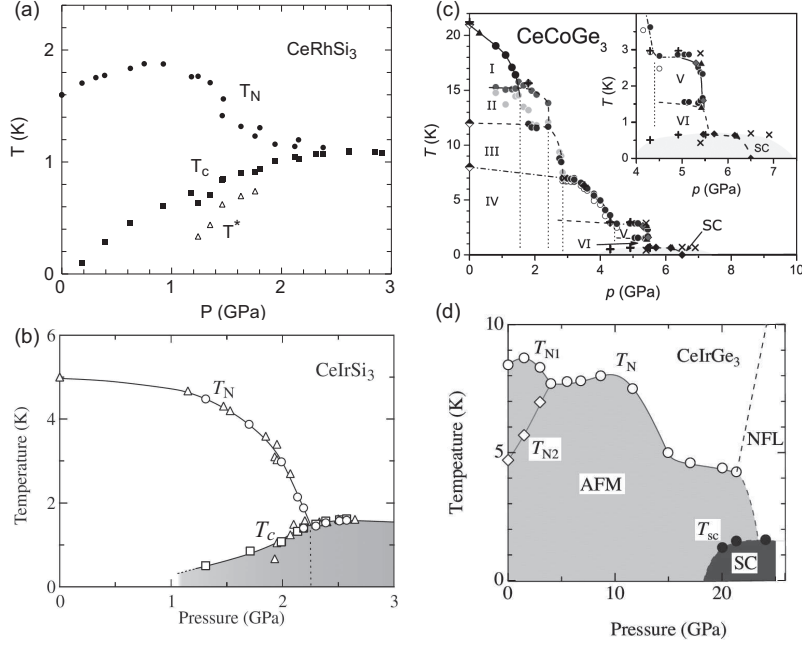


**Fig. 15** Temperature-pressure phase diagrams of CeRhSi<sub>3</sub> [72], CeIrSi<sub>3</sub> [75], CeCoGe<sub>3</sub> [77] and CeIrGe<sub>3</sub> [42].  $T^*$  in panel (a) denotes an anomaly observed in the resistivity and magnetic-susceptibility measurements [39].

below  $P_1^*$  is small and broad, while it becomes sharper with increasing pressure and is strongly enhanced above  $P_1^*$  [75]. In CeIrSi<sub>3</sub>, as shown in Fig. 16,  $\Delta C/C_n$ , where  $C_n$  is the normal state value just above  $T_c$ , reaches  $5.7 \pm 0.1$  at 2.58 GPa, which is much larger than the 1.43 value expected from the weak-coupling BCS model and is probably the highest value among all known superconductors. On the other hand, the jump of the heat capacity associated with antiferromagnetism diminishes when approaching  $P_1^*$ , and is no longer observed above  $P_1^*$ . Apparently, the entropy gain of the AFM transition is transferred to the superconducting one.

### 2.2.3 Quantum Criticality and Non-Fermi Liquid

Superconductivity in  $f$ -electron materials often appears in the vicinity of a quantum critical point (QCP) at which the magnetic ordering temperature is reduced to zero by a nonthermal control parameter such as pressure, magnetic field, or chemical substitution. Often, a QCP accompanies the emergence of a non-Fermi liquid in which the temperature dependence of some physical properties obeys different behavior from that expected in the Fermi-liquid theory. As shown in Fig. 17, the electrical resistivity changes from the Fermi-liquid prediction  $\rho(T) = \rho_0 + AT^2$  below  $P_1^*$  to  $\rho(T) = \rho_0 + A'T$  above  $P_1^*$  in CeRhSi<sub>3</sub> and CeIrSi<sub>3</sub> [40, 72]. A similar crossover oc-

**Table 3** Normal and superconducting parameters of  $\text{CeTX}_3$  compounds.  $\xi(0)$  is estimated from Eq. (5). Here, we regard  $H_{c2}(0)$  for  $H \parallel c$  as  $H_{orb}$ ; that is, the paramagnetic pair-breaking effect is absent.  $P_1^*$ ,  $P_2^*$  and  $P_3^*$  are the pressures at which  $T_N = T_c$ ,  $T_N \rightarrow 0$  and  $T_c$  reaches a maximum, respectively.  $\mathbf{q}$ ,  $\mathbf{m}_Q$  and  $\mu_s$  denote magnetic propagation vector, magnetic moment and value of ordered moment, respectively, and  $H'_{c2} \equiv -dH_{c2}/dT|_{T=T_c}$ .

	CeRhSi <sub>3</sub>	CeIrSi <sub>3</sub>	CeCoGe <sub>3</sub>	CeIrGe <sub>3</sub>
crystal structure			tetragonal	
space group			$I4mm$	
$a$ [Å]	4.237	4.252	4.320	4.401
$c$ [Å]	9.785	9.715	9.835	10.024
$\gamma_n$ [mJ/mol·K <sup>2</sup> ]	110	120	32	80
$m^*$ [ $m_0$ ]	4 – 19	N/A	N/A	N/A
$l$ [Å]	2400 – 3400	N/A	N/A	N/A
$T_N$ [K]	1.6	5.0	21/12/8	8.7/4.8
$\mathbf{q}$	(±0.215, 0, 0.5)	N/A	(0, 0, 1/2) (0, 0, 3/4)	N/A
$\mathbf{m}_Q$ orientation	[001]	[001]	[100]	[100]?
$\mu_s$ [ $\mu_B/\text{Ce}$ ]	0.13	N/A	0.5	N/A
$P_1^*$ (GPa)	2.4-2.5	2.25	5.5-5.6 <sup>d</sup>	> 21
$P_2^*$ (GPa)	?	2.50	5.5-5.7 <sup>d</sup>	~ 24
$P_3^*$ (GPa)	2.65	2.63	5.7 <sup>d</sup> or 6.5 <sup>e</sup>	≥ 24
$T_c @ P_3^*$ [K]	1.09	1.56 – 1.59	0.66 <sup>d</sup> or 0.69 <sup>e</sup>	≥ 1.6
$\Delta C/\gamma_n T_c$	N/A	5.7	N/A	N/A
$H_{c2}(0)$ [T] ( $H \parallel c$ )	30 ± 2 <sup>a</sup>	45 ± 10 <sup>c</sup>	22 ± 8 <sup>f,8</sup>	27 ± 10
$H_{c2}(0)$ [T] ( $H \perp c$ )	7.5 <sup>b</sup>	9.5 <sup>c</sup>	N/A	N/A
$\xi(0)$ [Å] ( $H \parallel c$ )	~ 33	~ 27	~ 39	~ 35
$H'_{c2}$ [T/K] ( $H \parallel c$ )	23 <sup>b</sup>	17 <sup>c</sup>	20 <sup>d</sup>	16 <sup>h</sup>
$H'_{c2}$ [T/K] ( $H \perp c$ )	27 <sup>b</sup>	14.5 <sup>c</sup>	N/A	N/A

<sup>a</sup> at 2.85 GPa

<sup>b</sup> at 2.6 GPa

<sup>c</sup> at 2.65 GPa

<sup>d</sup> determined from heat-capacity measurements[77].

<sup>e</sup> determined from electrical-resistivity measurements[43].

<sup>f</sup> at 6.5 GPa

<sup>g</sup> estimated from Fig. 25.

<sup>h</sup> at 24 GPa

curs in CeCoGe<sub>3</sub> at 6.9 GPa [43]. The  $T$ -linear dependence of the resistivity agrees with the prediction by the 2D spin fluctuation theory as indicated in Table 4. On the other hand, in CeIrSi<sub>3</sub>  $1/T_1$ -NMR measurements in the normal state reveal a  $\sqrt{T}$  dependence at 2.7 GPa for  $H \perp c$ . This supports a prediction for 3D AFM fluctuations in this system:  $1/T_1 \propto T \sqrt{\chi_Q(T)} \propto T/\sqrt{(T + \theta)}$  [78]. Here,  $\chi_Q(T)$ , the staggered susceptibility with the AFM propagation vector  $\mathbf{Q}$ , follows the Curie-Weiss law and  $\theta$  measures the deviation from the QCP. The specific heat divided by temperature  $C/T$  of CeIrSi<sub>3</sub> is estimated to be enhanced almost linearly with decreasing temperature from consideration of the entropy balance [75]. The enhancement of  $C/T$  is

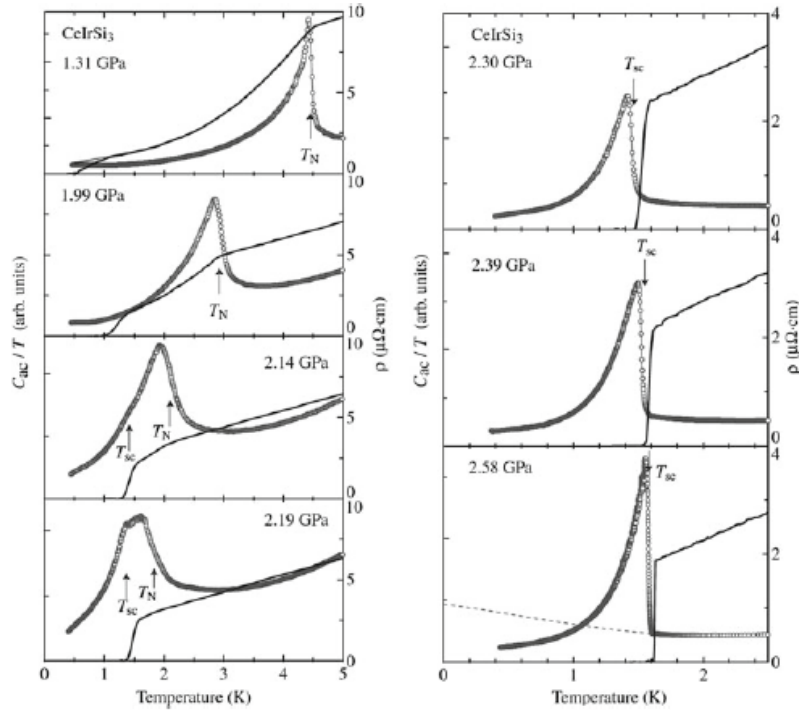


**Fig. 16** Temperature dependence of the ac heat capacity  $C_{ac}$  (circles, left side) and the electrical resistivity  $\rho$  (lines, right side) at several pressures in CeIrSi<sub>3</sub>. The dotted line in the panel at 2.58 GPa indicates the entropy balance below  $T_c$  [75].

consistent with the spin fluctuation theory, even though from theory we cannot determine the proper dimensionality. The contradiction in the temperature responses of  $\rho$  and  $1/T_1$  remains unsettled.

In general, it is unclear whether or not a QCP truly exists in CeT<sub>3</sub>, since the AFM transitions above  $P_1^*$  are prevented or masked by superconductivity. For example, the specific heat jump associated with the AFM transition seems to disappear suddenly just above  $P_1^*$  in CeIrSi<sub>3</sub> as mentioned above. This suggests that the QCP exists neither at  $P_2^*$  nor at higher pressures. However, this does not necessarily indicate that magnetic fluctuations vanish at these pressures. The fact that the maximum  $T_c$  and the sharpest resistivity drop take place at  $P_3^*$  implies that magnetic fluctuations survive even above  $P_1^*$  and rather develop toward  $P_3^*$ . Assuming that magnetic fluctuations stabilize the superconducting phase and become stronger at the QCP,  $P_3^*$  should be regarded as a *virtual* QCP.

In the vicinity of the QCP some pressure-induced HF superconductors display a strong enhancement of the effective mass of the conduction electrons; namely, via the  $\gamma_n$  value and the coefficient  $A$  of the  $T^2$  term of the electrical resistivity [79, 80, 81]. In the cases of CeRhSi<sub>3</sub> and CeIrSi<sub>3</sub>, however, such an enhancement is less obvious. The coefficient  $A$  in CeRhSi<sub>3</sub> is almost constant up to  $P_1^*$  [72] and

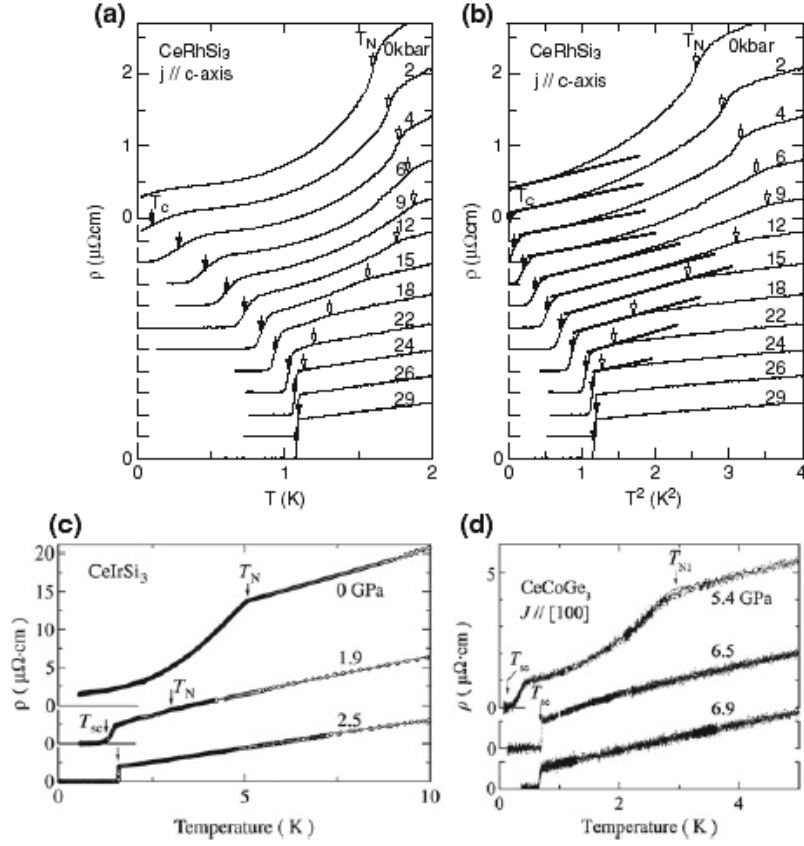


**Fig. 17** Temperature dependence of the resistivity of (a) CeRhSi<sub>3</sub> [72], (c) CeIrSi<sub>3</sub> [40] and (d) CeCoGe<sub>3</sub> [43]. (b) Resistivity against  $T^2$  in CeRhSi<sub>3</sub>.

the  $\gamma_n$  value in CeIrSi<sub>3</sub> is suggested to be unchanged up to  $P_3^*$  [75]. On the other hand, the coefficient  $A$  in CeCoGe<sub>3</sub> is strongly enhanced from  $0.011 \mu\Omega\text{-cm}/\text{K}^2$  at ambient pressure to  $0.357 \mu\Omega\text{-cm}/\text{K}^2$  at 5.4 GPa. In CeIrGe<sub>3</sub>  $\rho(T)$  exhibits a complicated pressure dependence (as shown in Fig. 18) that makes unclear how  $A$  varies with pressure. The drastic changes at certain pressures between 8.6 GPa and 17 GPa may be associated with the step-like decrease of  $T_N(P)$  around 13 GPa as seen in Fig. 15(d). The residual resistivity becomes maximum at a pressure near 17 GPa. Since such an enhancement of residual resistivity can be a signature of critical valence fluctuations [82], a valence transition or crossover may take place around 13 GPa in CeIrGe<sub>3</sub>.

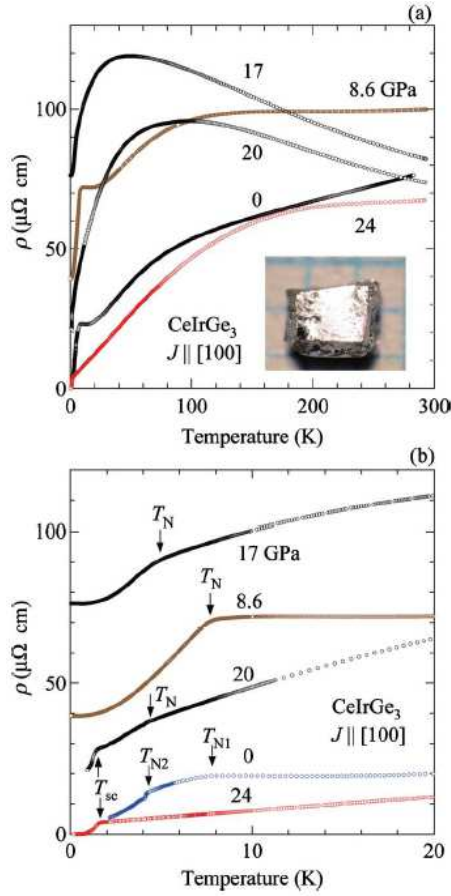


**Fig. 18** Temperature dependence of the resistivity of  $\text{CeIrGe}_3$  at several pressures up to 24 GPa (a) below room temperature and (b) below 20 K [42].

## 2.3 Superconducting State

### 2.3.1 Anisotropic Upper Critical Field : Two Limiting Fields

Thus far, the most interesting phenomenon in the  $\text{CeTX}_3$  superconductors is the extremely high anisotropy in the upper critical magnetic field  $H_{c2}$ , with stunningly high values for fields along the  $c$  axis. In  $\text{CeRhSi}_3$  and  $\text{CeIrSi}_3$ , for example,  $H_{c2}$  exceeds 30 T along the  $c$  axis, whereas falls below 10 T along the plane. Considering that in these materials  $T_c$  is of the order of 1 K, this leads to very high  $H_{c2}/T_c$  ratios not known previously for any *centrosymmetric* superconductors (except for field-induced superconductors like  $\text{URhGe}$  [83] and organic superconductors [84]). The strong field anisotropy and the extremely high  $H_{c2}$ s are thought to be understood

**Table 4** Theoretically predicted quantum critical behavior for 3D and 2D antiferromagnetic fluctuations and corresponding temperature dependence on  $CeTX_3$  compounds.

	$\rho$	$1/T_1$	$C/T$
3D AFM	$T^{3/2}$	$T/\sqrt{T+\theta}$	const. $-T^{1/2}$
2D AFM	$T$	$T/(T+\theta)$	$-\ln T$
CeRhSi <sub>3</sub>	$T$ [39]		
CeIrSi <sub>3</sub>	$T$ [40]	$T/\sqrt{T+\theta}$ [78]	$T$ ? [75]
CeCoGe <sub>3</sub>	$T$ [43]		
CeIrGe <sub>3</sub>	$T$ [42]		

in terms of the anisotropy of the paramagnetic pair-breaking effect characteristic of non-centrosymmetric (Rashba-type) superconductors.

There are two pair-breaking mechanisms for Cooper pairs under magnetic fields: the paramagnetic and the orbital. The former mechanism is attributed to the spin polarization due to the Zeeman effect, which competes with the antiparallel-spin formation of the Cooper pair in spin-singlet superconductors. The influence of the paramagnetic effect depends on the symmetry of the Cooper pairs, as discussed later. On the other hand, the orbital effect is ascribed to the orbital motion in a magnetic field. The influence of this effect is thought to be independent of the pairing symmetry. The magnitude of  $H_{c2}(0)$  is consequently restricted by both the paramagnetic (Pauli-Clogston-Chandrasekhar) limiting field  $H_P$  and the orbital limiting field  $H_{orb}$  [85]. Hereafter, we call  $H_P$  the Pauli limiting field for simplicity.

#### Pauli-Clogston-Chandrasekhar limit

The paramagnetic effect in spin-singlet and spin-triplet pairing symmetries is illustrated schematically in Fig. 19. In centrosymmetric superconductors, the up-spin and down-spin bands of the conduction electrons are degenerate in zero field. The corresponding Fermi surfaces are also degenerate. The presence of a magnetic field inflates and deflates the down-spin and up-spin Fermi surfaces, respectively, due to the Zeeman effect. When the Cooper pair consists of antiparallel spins, e.g. the conventional singlet pair, the paramagnetic pair breaking occurs on the whole Fermi surface. When the Cooper pair comprises parallel spins, namely the triplet pair, the paramagnetic pair breaking does not occur, therefore the Pauli limit is absent. Since the spin direction of the Cooper pair is always aligned to the magnetic field, both cases are independent of the field direction unless the coupling between the orbital and spin parts of the pairing function is present.

In non-centrosymmetric superconductors, the up-spin and down-spin Fermi surfaces are not degenerate even in zero field. In the Rashba-type (tetragonal) superconductors, the spins are perpendicularly aligned with the momenta in the  $k_z$  plane (Fig. 19) by the spin-orbit coupling, yielding a momentum-dependent effective magnetic field. The presence of an applied magnetic field along the  $k_x$  direction inflates and deflates the Fermi surfaces only along the  $k_y$  direction, since the spin component perpendicular to the  $k_x$  direction is not affected by this field. The paramagnetic pair-



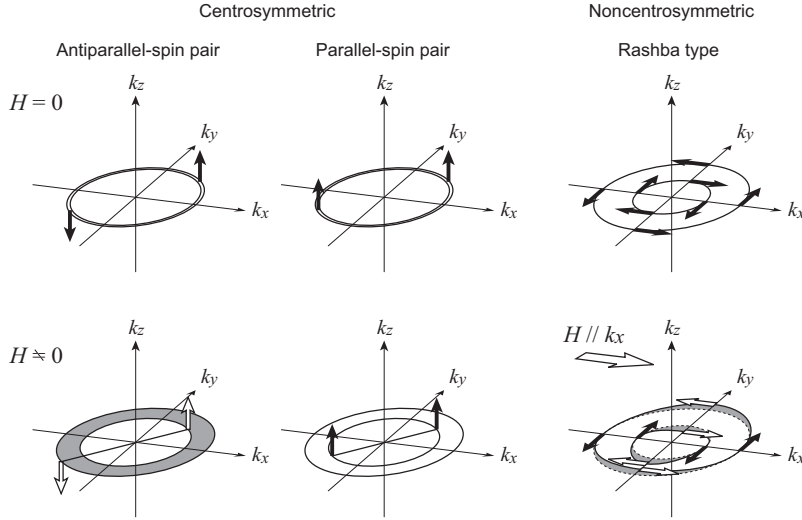


**Fig. 19** Two-dimensional Fermi surfaces for centrosymmetric and non-centrosymmetric superconductors at zero and finite fields. The centrosymmetric superconductors can be classified into parallel- and antiparallel-spin pairs. In the non-centrosymmetric superconductor, only the Rashba type is displayed. The hollow arrows indicate a pairing no longer allowed. In the antiparallel-spin pair including the conventional singlet pair, the pair breaking occurs on the whole Fermi surface under magnetic fields. On the other hand, in the parallel-spin pair, all the pairing persist. In the Rashba-type superconductor, pair breaking occurs only for the pairs parallel to the applied magnetic field. When the magnetic field is applied to  $k_z$ , pair breaking does not occur.

breaking effect is thus partial for field along the  $k_z$  plane. On the other hand, when the magnetic field is applied along the  $k_z$  axis, the paramagnetic pair-breaking effect is absent because all the spins aligned with the  $k_z$  plane are perpendicular to the field direction. The strongly anisotropic  $H_{c2}(T)$ , with high  $H_{c2}(0)$  for  $H \parallel c$ , realized in  $\text{CeTX}_3$  compounds is attributed to the anisotropic spin susceptibility expected to appear in non-centrosymmetric superconductors as discussed above in Spin State, Sect. 1.3.1.

Figure 20 shows  $H_{c2}(0)$  versus  $T_c$  for  $\text{CeTX}_3$  compounds and some well-known HF superconductors. The dashed line indicates  $H_P^{\text{BCS}}$  (see Eq. 4). The  $H_{c2}(0)$  of the U-based superconductors  $\text{UGe}_2$ ,  $\text{URhGe}$  and  $\text{UPt}_3$  exceeds  $H_P^{\text{BCS}}$ . These superconductors are thought to form a parallel-spin pairing free from the paramagnetic pair-breaking effect. In some spin-singlet superconductors  $H_{c2}(0)$  is located above the  $H_P^{\text{BCS}}$  line, which seems a contradiction. Two possibilities have been proposed: one is a reduction of the  $g$ -factor and the other is an enhancement of  $\Delta_0$  due to a strong-coupling effect.  $H_{c2}(0)$ s of  $\text{CeTX}_3$  compounds do not only exceed the  $H_P^{\text{BCS}}$  line, but also surpass those of all other materials. To understand the high  $H_{c2}$  of the  $\text{CeTX}_3$  compounds, it is necessary to consider the orbital pair-breaking effect that we discuss next.

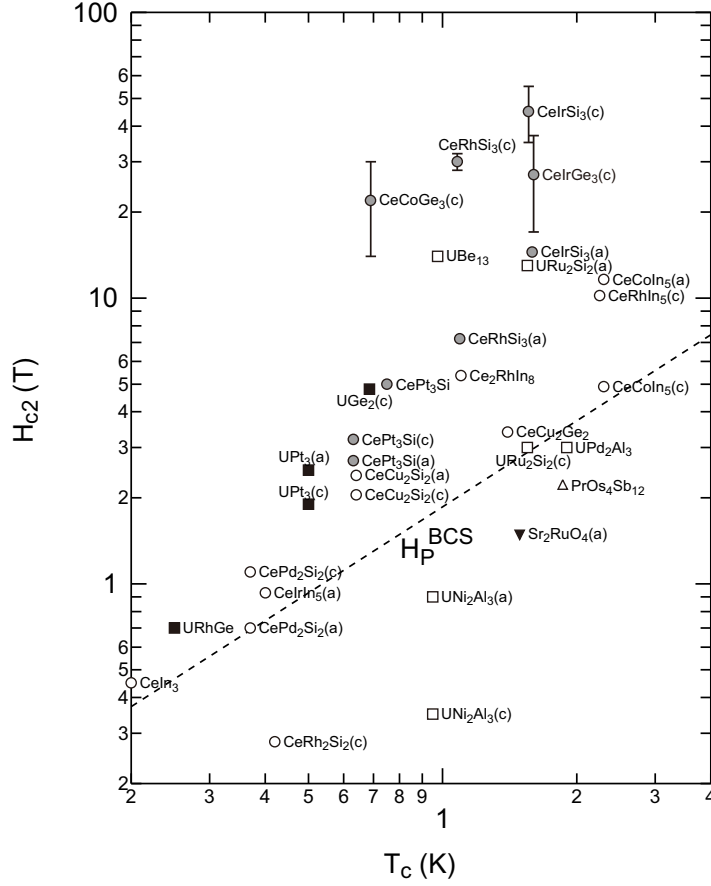


**Fig. 20**  $H_{c2}(0)$  versus  $T_c$  for heavy-fermion and some other well-known superconductors. The broken line represents  $H_P^{\text{BCS}} = 1.86T_c$ . The circles, squares and upper and lower triangles indicate cerium, uranium, praseodymium and other compounds, respectively. The solid and hollow symbols tag possible triplet and singlet (or unclear) superconductors, respectively. The gray marks label non-centrosymmetric superconductors. The letter *a* or *c* in parentheses denotes the applied field direction and no letter indicates that the result was obtained for a polycrystal.

### Orbital limit

As we discussed above, the orbital limiting field can be estimated from Eq. (6). The value  $h(0)$  depends on both the ratio  $\xi(0)/l$  and the strong-coupling parameter  $\lambda$  ( $l$ : mean free path). In the weak-coupling limit ( $\lambda = 0$ ), namely the BCS model,  $h(0) = 0.727$  for  $(\xi(0)/l) \rightarrow 0$  (clean limit) and  $h(0) = 0.693$  for  $(\xi(0)/l) \rightarrow \infty$  (dirty limit). Most HF superconductors satisfy the clean limit. In the strong-coupling limit ( $\lambda \rightarrow \infty$ ),  $h(0)$  approaches 1.57 for clean superconductors [86] and increases with  $\lambda$  for dirty superconductors. It is noted that the  $\lambda$  dependence of  $h$  is usually derived on the basis of the conventional electron-phonon model, but that in HF systems a

corresponding electron-magnon approach should be employed since it is generally believed that the attractive interaction leading to Cooper pairs arises from coupling to spin excitations.

The  $H_{c2}(0)$ s in Fig. 20 are plotted against  $H'_{c2}T_c$  in Fig. 21. The dashed and dotted lines indicate the orbital limiting fields at  $\lambda = 0$  (weak-coupling limit) and  $\lambda \rightarrow \infty$  (strong-coupling limit) for clean superconductors; that is,  $H_{orb}^{BCS} = 0.727H'_{c2}T_c$  and  $H_{orb}^{\infty} = 1.57H'_{c2}T_c$ , respectively. Some parallel-spin, namely triplet, superconductors like UPt<sub>3</sub> and URhGe are located just below  $H_{orb}^{BCS}$ . The compounds located far below the  $H_{orb}^{BCS}$  line in Fig. 20, e.g. UNi<sub>2</sub>Al<sub>3</sub> and CeRh<sub>2</sub>Si<sub>2</sub>, are seen in the vicinity of the  $H_{orb}^{BCS}$  line in Fig. 21. The  $H_{c2}$ s of these compounds may be mainly restricted by the orbital limit rather than by the Pauli limit. CePt<sub>3</sub>Si is also located near the  $H_{orb}^{BCS}$  line. Considering that  $H_{c2}$  is almost isotropic in CePt<sub>3</sub>Si [10], it may be also mainly constrained by the orbital limit rather than by the paramagnetic one.

The  $H_{c2}$ s of the CeTX<sub>3</sub> compounds for fields along the  $c$  axis well exceed the  $H_{orb}^{BCS}$  line. They seem to be close to the strong-coupling limit  $H_{orb}^{\infty}$ . Although the high  $H_{c2}/(H'_{c2}T_c)$  is a common feature in the CeTX<sub>3</sub> HF superconductors, it is not obvious that such a result can be associated with their non-centrosymmetric crystal structures. Note that UGe<sub>2</sub> also seems to be above the  $H_{orb}^{BCS}$  line, but this is due to the jump of the  $H_{c2}$  curve attributed to the metamagnetic transition [87, 88]. Therefore, this plot does not necessarily indicate that the intrinsic  $H_{c2}(0)$  of UGe<sub>2</sub> exceeds the  $H_{orb}^{BCS}$  line.

### 2.3.2 Upper Critical Field for $c$ axis

In addition to the high values of  $H_{c2}(0)$ , the upward shape of the temperature dependence of  $H_{c2}(T)$  for certain pressures seems to be also a characteristic of the CeTX<sub>3</sub> superconductors [43, 54, 72]. They mostly keep a positive curvature ( $d^2H_{c2}/dT^2 > 0$ ) down to relatively low temperatures; for example, in CeIrSi<sub>3</sub> down to  $T \approx 0.25T_c$  at 2.6 GPa (Fig. 23). Interestingly, the curve shapes of CeRhSi<sub>3</sub> and CeIrSi<sub>3</sub> vary with pressure in a complex manner. As for CeIrSi<sub>3</sub>, a positive curvature is seen up to 2 GPa that gradually changes to a negative curvature at 2.4 GPa to a quasi-linear shape at 2.3 GPa. At 2.6 GPa and 2.65 GPa, a positive curvature is recovered that turns to a negative one at higher pressures. Similar behavior is seen in CeRhSi<sub>3</sub>. Below and above 2.6 GPa, the curvatures of  $H_{c2}(T)$  are positive. At 2.6 GPa, a quasi-linear change of  $H_{c2}(T)$  is observed. Because of the lack of sufficient pressure data, it is not clear whether such a phenomenon is realized in CeCoGe<sub>3</sub> and CeIrGe<sub>3</sub>.

In order to understand the superconducting phase diagram of the CeTX<sub>3</sub> compounds the pressure dependence of  $H_{c2}(0)$  will be very helpful. Fig. 22(c) shows  $H_{c2}(0)$  versus pressure in CeIrSi<sub>3</sub> [54].  $H_{c2}(0)$  increases with pressure and tends to diverge close to 2.65 GPa ( $\approx P_3^*$ ). Above 2.65 GPa it falls steeply to half or less of the value of the maximum  $H_{c2}(0)$ . It is pointed out that such an acute enhancement of  $H_{c2}(0)$  can be interpreted as an electronic instability arising at  $P_3^*$  [54]. This instability can cause a mass enhancement of the conduction electrons, giving rise to

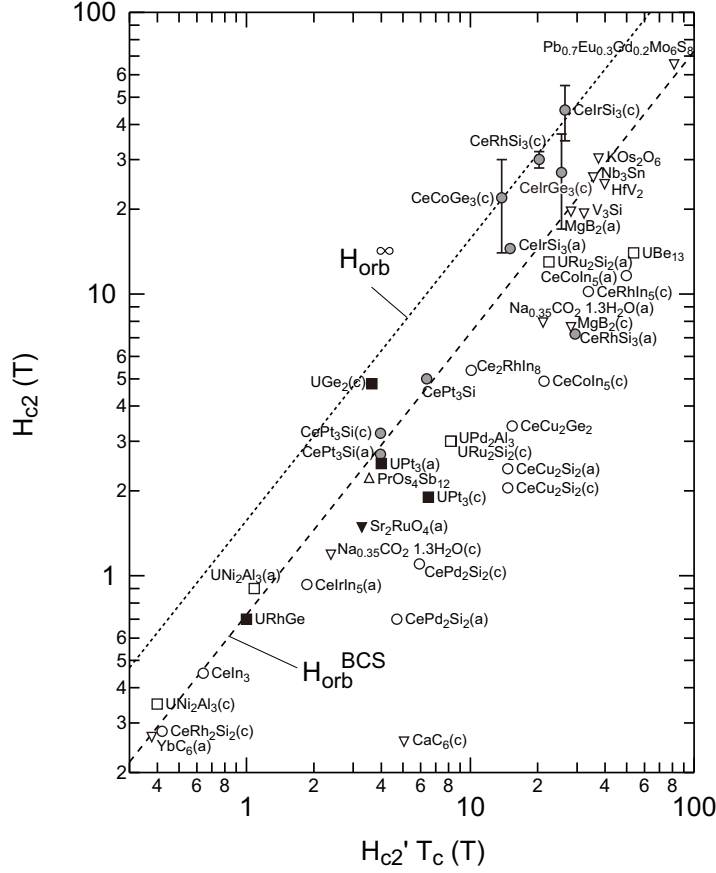


**Fig. 21**  $H_{c2}(0)$  versus  $H'_{c2}T_c$  for heavy-fermion and other well-known superconductors. The broken and dotted lines represent  $H_{orb}^{BCS} = 0.727H'_{c2}T_c$  and  $H_{orb}^{\infty} = 1.57H'_{c2}T_c$ , respectively. The circles, squares and upper and lower triangles indicate cerium, uranium, praseodymium and other compounds, respectively. The solid and hollow symbols tag possible triplet and singlet (or unclear) superconductors, respectively. The gray marks label non-centrosymmetric superconductors. The letter *a* or *c* in parentheses denotes the applied field direction and no letter indicates that the result was obtained for a polycrystal.

a reduction in the superconducting coherence length  $\xi(0)$ . At a first glance, a mass enhancement at  $P_3^*$  is consistent with the pressure dependence of the initial slope of the superconducting  $H$ - $T$  phase diagram,  $H'_{c2} = -dH_{c2}/dT|_{T=T_c}$ . From Eqs. (5) and (6), we can derive

$$H'_{c2}T_c \sim H_{orb} \sim \xi^{-2}(0) \sim (\Delta_0 m^*)^2. \quad (10)$$

Here, we use  $v_F = \hbar k_F/m^*$ . As shown in Figs. 23 - 25,  $H'_{c2}$ s of CeIrSi<sub>3</sub> and CeRhSi<sub>3</sub> increase with increasing pressure and become maximum at about  $P_3^*$ . However,

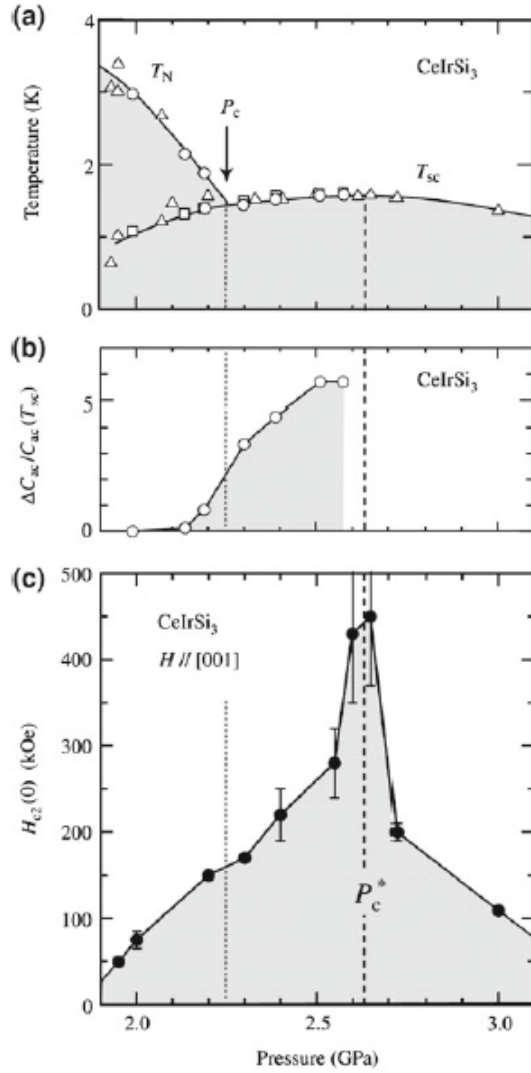


**Fig. 22** Pressure dependence of (a)  $T_N$  and  $T_c$ , (b) specific heat jump  $\Delta C/C(T_c)$  and (c)  $H_{c2}(0)$  for  $H \parallel c$  in CeIrSi<sub>3</sub> [54].

strong pressure dependence of the cyclotron effective mass is not observed in de Haas-van Alphen experiments in CeRhSi<sub>3</sub> [89]. This is consistent with the result of the less obvious pressure dependence of the resistivity coefficient  $A$ . A small enhancement of the effective mass is also suggested by heat-capacity measurements in CeIrSi<sub>3</sub> [75].

In order to explain the positive curvature of  $H_{c2}(T)$  and the strong pressure dependence of  $H_{c2}(0)$ , Tada *et al.* considered the temperature and pressure dependen-

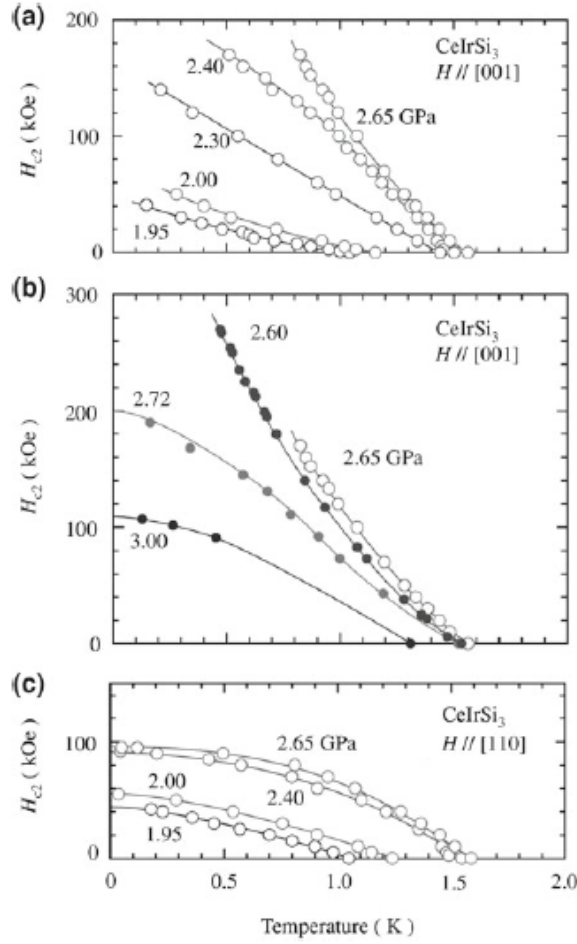


**Fig. 23**  $H_{c2}$ - $T$  phase diagrams of  $\text{CeIrSi}_3$  for  $H \parallel c$  at  $P \leq P_3^* \approx 2.65$  GPa (a), at  $P \geq P_3^*$  (b), and for  $H \perp c$  at  $P \leq P_3^*$  [54].

cies of the correlation length of the spin fluctuations,  $\xi_{sf}$ , [90]. Since  $\xi_{sf}$  is expressed as  $\xi_{sf}(T) = \frac{\xi_{sf}}{\sqrt{T+\theta}}$ , in which  $\theta \rightarrow 0$  toward the QCP and the effective pairing interaction is quadratically proportional to  $\xi_{sf}$ , the superconducting coherence length  $\xi(0)$  is strongly reduced and  $H_{orb}$  enhanced at low temperatures. This model can explain the enhancement of the initial slope and is compatible with the weaker enhancement of the effective mass.

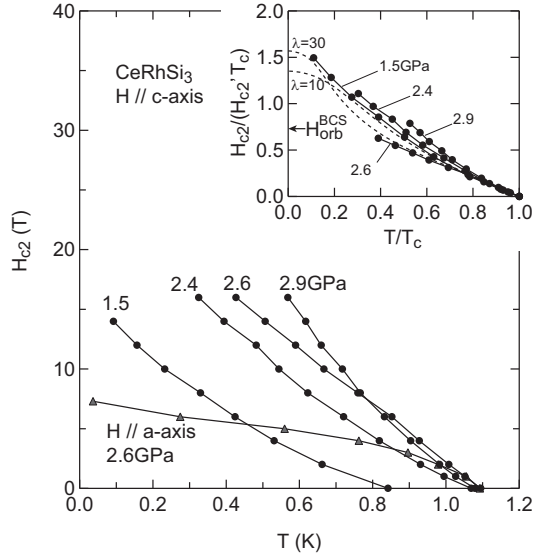


**Fig. 24**  $H_{c2}$ - $T$  phase diagrams of  $\text{CeRhSi}_3$  for  $H // c$  at several pressures and for  $H // a$  at  $P_3^* \approx 2.6$  GPa. Inset:  $H_{c2}(T)$  curves for  $H // c$  normalized by the initial slope. The arrow indicates the orbital limit  $H_{orb}^{BCS}$ . The dashed curves are theoretical predictions based on the strong-coupling model using the coupling strength parameter  $\lambda = 10$  and  $30$  [93].

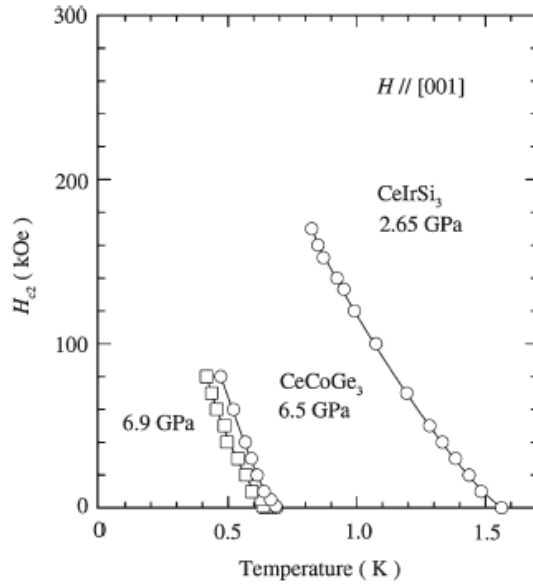


**Fig. 25**  $H_{c2}$ - $T$  phase diagram of  $\text{CeCoGe}_3$  for  $H // c$  at 6.5 GPa and 6.9 GPa. The phase diagram of  $\text{CeIrSi}_3$  is also displayed [43].

### 2.3.3 Superconducting Phase Diagram for Field in the Basal Plane

In contrast to the high  $H_{c2}(T)$  for the  $c$  axis,  $H_{c2}(T)$  in the basal plane is not too high. However, it still significantly exceeds  $H_p^{\text{BCS}}$  and is situated in the upper part of Fig. 20. As discussed in the section above, the high  $H_{c2}(0)$  is attributed to the reduced paramagnetic pair-breaking effect which originates mainly from a non-vanishing spin susceptibility. In addition to this, Agterberg *et al.* pointed out that another characteristic mechanism, the helical vortex state, can also evade the paramagnetic pair-breaking effect when the magnetic field is applied in the basal plane [91, 92].

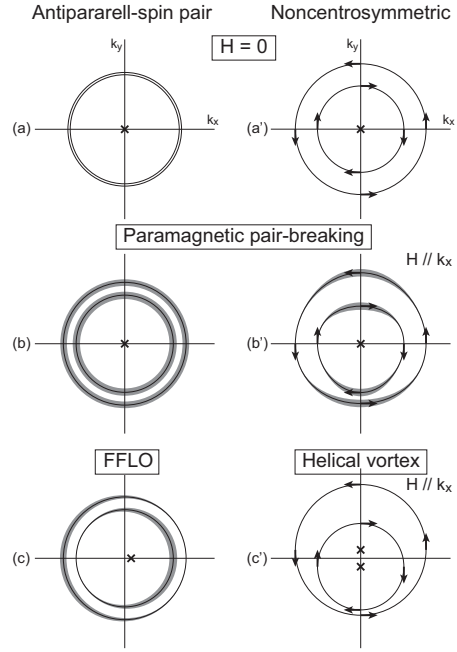


**Fig. 26** Schematic illustrations of Fermi surface sliced perpendicular to the  $k_z$  axis. Pair breaking takes place at the shaded region. The x marks indicate the positions of the center-of-mass momenta of the Cooper pairs.

As discussed above, the paramagnetic pair-breaking effect operates partially, with the center-of-mass momentum of the Cooper pair remaining zero at any  $k$  as shown in Fig. 26(b). On the other hand, in the helical vortex state, the Fermi surfaces shift toward opposite directions perpendicular to the field direction. An application of a magnetic field does not break the Cooper pairs for all  $k$ . In this case, the center-of-mass momenta of the Cooper pairs belonging to each Fermi surface acquire a finite value  $\pm q$  (Fig. 26(c)). The sign of  $q$  depends on the Fermi surface. In the Fulde-Ferrel-Larkin-Ovchinnikov (FFLO) state, a Cooper pair with a finite center-of-mass momentum is also realized. However, the pairing takes place in a limited region on the Fermi surface. In other regions, indicated by the shades in Fig. 26(c), pairing is not allowed. Since both states, helical vortex and FFLO phase, evade the paramagnetic pair breaking, relatively high  $H_{c2}(0)$  can be realized.



Although thus far no direct evidence for a helical vortex state has been detected in either  $CeTX_3$  compounds or  $CePt_3Si$ , some unusual superconducting properties for the field in the basal plane are reported in  $CeRhSi_3$  [39]. First, there is a concave shape of the  $H_{c2}(T)$  curve as shown in Fig. 27(a). The rapid change of  $H_{c2}$  at low

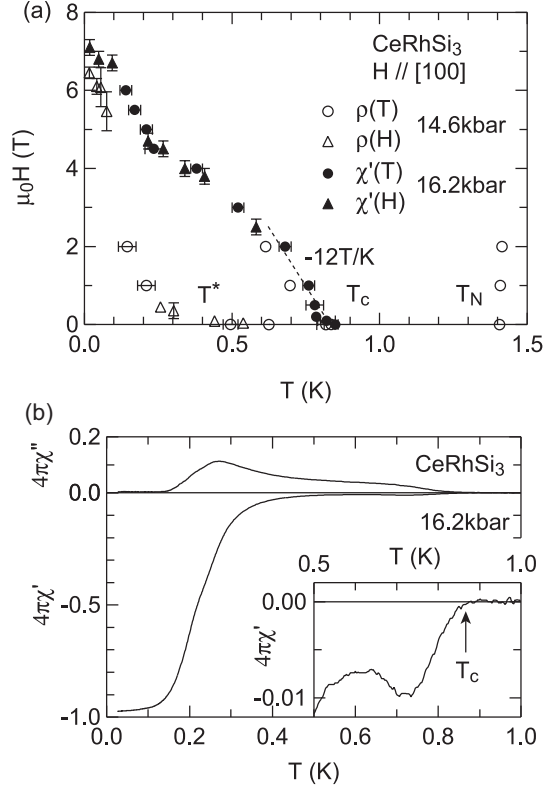


**Fig. 27** (a) Magnetic field-temperature phase diagram of  $CeRhSi_3$  for  $H \parallel a$  below  $P_1^*$ .  $T^*$  denotes the temperature at which an anomaly is observed in the resistivity and magnetic ac susceptibility measurements. (b) ac susceptibility as a function of temperature at zero field below  $P_1^*$ . An enlarged view of the vicinity of  $T_c$  is shown in the inset [39].

temperatures looks similar to the one observed in a theoretically predicted helical-vortex phase diagram [92]. However, this feature observed at  $P < P_1^*$  becomes less obvious at  $P_3^* \approx 2.6$  GPa [72]. An influence of the antiferromagnetic order to explain this unusual curve shape cannot be excluded. Second, the ac susceptibility in the superconducting state shows an unusual shape especially below  $P_1^*$ . The temperature at which a large drop occurs in the real part of the susceptibility  $\chi'$  is far below the onset temperature of superconductivity. This might indicate that superconductivity develops gradually in the antiferromagnetic state. On the other hand, the imaginary part  $\chi''$ , namely the energy dissipation associated with the dynamics of the superconducting flux, is large even above the temperature at which the large drop occurs in  $\chi'$ . This contradicts the view of a gradual development of superconductivity. Although the influence of antiferromagnetism is unclear at present, this rare behavior of the flux may be a key feature to verify the helical vortex state.

### 2.3.4 Energy Gap Structure and Pairing Symmetry

In CeIrSi<sub>3</sub> the nuclear spin-lattice relaxation rate  $1/T_1$  shows a  $T^3$ -like dependence below  $T_c$  without a coherence peak, as shown in Fig. 28 [78]. The data are well fitted by the line-node gap model  $\Delta = \Delta_0 \cos 2\theta$ . The fit yields  $2\Delta_0/k_B T_c \approx 6$ , which is much larger than the BCS weak-coupling value 3.53 and thus suggests strong-coupling superconductivity. Using an extended  $s + p$  pairing state within a recent theoretical model a behavior indicative of a line-node gap can be predicted [94]. This

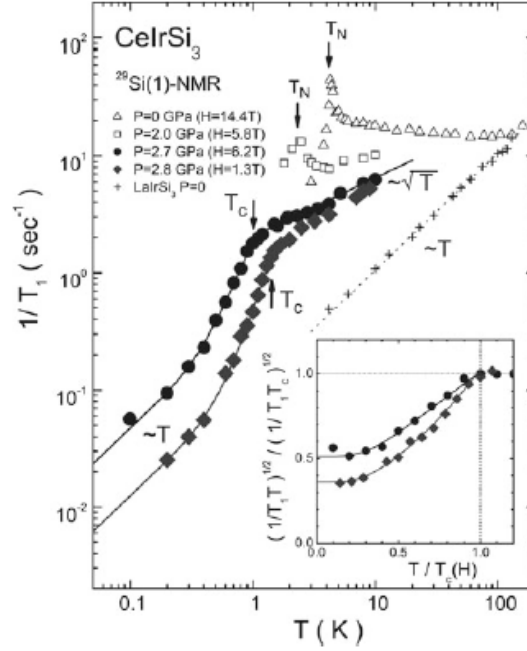


**Fig. 28** Temperature dependence of  $1/T_1$  measured by Si NMR for CeIrSi<sub>3</sub> at several pressures. The solid curves below  $T_c$  for CeIrSi<sub>3</sub> indicate the calculated values obtained by the line-node gap model with  $2\Delta_0/(k_B T_c) \approx 6$  and the residual density-of-states fraction  $N_{\text{res}}/N_0 \approx 0.37$  (0.52) in  $H = 1.3$  T (6.2 T). The inset shows the plot of  $\sqrt{1/(T_1 T)}$  normalized by that at  $T_c$  which allows us to evaluate  $N_{\text{res}}/N_0$  in the low-temperature limit [78].

$1/T_1$ -NMR measurement is the only one carried out to determine the energy gap structure in  $\text{CeTX}_3$  compounds. To identify the pairing symmetry in these materials, other measurements, like the Knight shift, are highly desirable.

## 2.4 Outlook

The high anisotropy and strong enhancement of  $H_{c2}$  seem to be unique to  $\text{CeTX}_3$  superconductors. Interestingly, other HF and non-HF superconductors without inversion symmetry do not show these properties. The high orbital limiting field inherent to the non-centrosymmetric HF  $\text{CeTX}_3$  superconductors discloses the absence of the paramagnetic pair-breaking effect. Conversely, absence of the effect unveils the

unconventional nature of the upper critical fields probably associated with the quantum criticality of magnetism.  $CeTX_3$  compounds have the potential to provide a vital clue to the underlying mechanism of superconductivity mediated by magnetic fluctuations.

To consider the relation between magnetism and superconductivity in  $CeTX_3$ , we need to keep in mind that the magnetic ground states of  $CeCoGe_3$  and  $CeIrGe_3$  are different from that of  $CeRhSi_3$  and probably of  $CeIrSi_3$ .  $CeCoGe_3$  seems to display localized  $f$ -electron magnetism, while  $CeRhSi_3$  probably exhibits itinerant-electron magnetism. It is very interesting that in these compounds the  $H_{c2}$  behaviors are similar in spite of their different magnetism. The mass enhancement at  $P_3^*$  is suggested only in  $CeCoGe_3$ . The comparison of the superconducting properties of  $CeCoGe_3$  and  $CeIrGe_3$  with those of  $CeRhSi_3$  and  $CeIrSi_3$  will be important to elucidate the nature of HF superconductors. Identification of the gap structure in each compound is also a challenging issue, which could provide possible evidence for the parity mixing of the superconducting wavefunction. Moreover, some theoretically predicted phenomena, like a helical vortex phase and a novel magnetoelectric effect, remain to be verified in the future.

### 3 UIr

Whereas  $CeRhSi_3$ ,  $CeIrSi_3$ ,  $CeCoGe_3$ ,  $CeIrGe_3$  and  $CePt_3Si$  are  $4f$ -electron anti-ferromagnets, UIr is a  $5f$ -itinerant-electron ferromagnet with a Curie temperature  $T_{c1} = 46$  K at ambient pressure [95]. The superconducting state in UIr appears to develop within a higher pressure ferromagnetic phase at a critical temperature  $T_c = 0.14$  K in a narrow pressure region around 2.6 GPa [96]. UIr is a moderate heavy-fermion compound with a cyclotron mass  $m^* \sim 10 - 30 m_0$  [97]. The coexistence of superconductivity and ferromagnetism imposes several theoretical challenges, such as the mechanism and the state of pairing. The pairing state in superconducting ferromagnets needs to be spin triplet, otherwise the internal exchange field would break the Cooper pairs. On the other hand, a ferromagnetic state has a broken time reversal symmetry. The superconducting BCS ground state is formed by Cooper pairs with zero total angular momentum. The electronic states are four-fold degenerate:  $|\mathbf{k} \uparrow\rangle$ ,  $|\mathbf{k} \downarrow\rangle$ ,  $|\mathbf{-k} \uparrow\rangle$  and  $|\mathbf{-k} \downarrow\rangle$  have the same energy  $\varepsilon(\mathbf{k})$ . The states with opposite momenta and opposite spins are transformed to one another under time reversal operation  $\hat{K}|\mathbf{k} \uparrow\rangle = |\mathbf{-k} \downarrow\rangle$ , and the states with opposite momenta are transformed to one another under inversion operation  $\hat{I}|\mathbf{k} \downarrow\rangle = |\mathbf{-k} \downarrow\rangle$ . The four degenerate states are a consequence of spatial and time inversion symmetries. Parity symmetry is irrelevant for spin-singlet pairing, but is essential for spin-triplet pairing. Time reversal symmetry is required for spin-singlet configuration, but is unimportant for spin-triplet state [98, 99]. In UIr the lack of spatial and time inversion symmetries lifts the degeneracies and, therefore, superconductivity is not expected to occur. Thus, UIr differs from the other two known ferromagnetic superconductors  $UGe_2$  [100] and  $URhGe$  [101], in which the spatial inversion sym-

metry allows degeneracy in the spin-triplet states. Theoretically and experimentally UIr is a very special and challenging superconductor.

### 3.1 Crystal Structure and Characteristic Parameters

UIr crystallizes in a monoclinic PbBi-type structure (space group  $P2_1$ ) without inversion symmetry [95]. The lattice parameters are given in Table 5. The unit cell has eight formula units with four inequivalent U and Ir sites. The absence of inversion symmetry comes from the missing mirror plane  $(0, \frac{1}{2}, 0)$  perpendicular to the  $b$  axis (see Fig. 29). Magnetism is of the Ising type with the ordered magnetic moment oriented along the spin easy axis  $[10\bar{1}]$  (Fig. 29).

Single crystals of UIr have been grown by the Czochralski method in a tetra-arc furnace [102, 103, 104, 105, 106]. After annealing, using the solid-state electrotransport technique under high vacuum of the order of  $10^{-10}$  Torr, crystals become of very high quality with residual resistivity  $\rho_0 \sim 0.5 \mu\Omega$  and residual resistivity ratio (RRR)  $\rho_{300K}/\rho_0 \approx 200$  at ambient pressure. Interestingly, single crystals of UIr seem to be of the highest quality amongst those of non-centrosymmetric heavy-fermion superconductors.

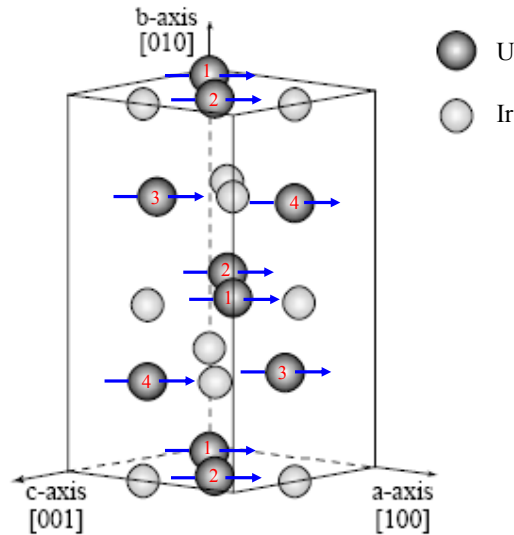


Fig. 29 Crystal and magnetic structures of UIr.

**Table 5** Normal and superconducting parameters of UIr

Crystal structure	monoclinic
Space group	$P2_1$
Lattice parameters	$a = 5.62 \text{ \AA}$ $b = 10.59 \text{ \AA}$ $c = 5.60 \text{ \AA}$ $\beta = 98.9^\circ$
Sommerfeld value of specific heat	$\gamma_n = 40 - 49 \text{ mJ/molK}^2$
Effective electron mass (Fermi sheet $\alpha$ )	$m^* \sim 10 - 30 m_0$
Mean free path (Fermi sheet $\alpha$ )	$l = 1270 \text{ \AA}$
Ferromagnetic transition temperature (ambient pressure)	$T_{c1} = 46 \text{ K}$
Magnetic propagation vector	$\mathbf{q} = (1, 0, -1)$
Magnetic moment $\mathbf{m}_Q$ along	$[10\bar{1}]$
Saturated moment per U atom	$\mu_s = 0.5 \mu_B$
Superconducting transition temperature	$T_c = 0.14 \text{ K}$
Upper critical field	$H_{c2}(0) = 26 \text{ mT}$
Thermodynamic critical field	$H_c(0) = 8 \text{ mT}$
Ginzburg-Landau coherence length	$\xi(0) = 1100 \text{ \AA}$
Ginzburg-Landau parameter	$\kappa \sim 2$

### 3.2 Normal State

#### 3.2.1 Phase Diagram and Magnetic Properties

Figure 30 shows the temperature-pressure phase diagram as drawn by magnetization and resistivity measurements [96]. The diagram consists of a low-pressure ferromagnetic phase FM1 ( $F_1$  in the figure), a high-pressure ferromagnetic phase FM2 ( $F_2$  in the figure), and a superconducting phase UIr.

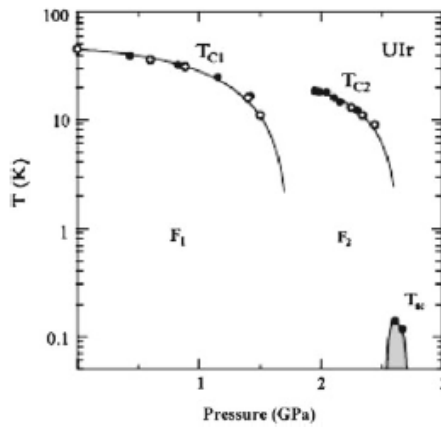


**Fig. 30** Temperature-pressure phase diagram of UIr [96].  $F_1$  and  $F_2$  are ferromagnetic phases.

( $F_2$  in the figure) and a superconducting phase. A third magnetic phase was reported [107], but not further evidence for it has been found. Application of pressure decreases the Curie temperature  $T_{c1}$  of the ferromagnetic phase FM1 eventually to zero at the critical pressure  $P_{c1} \sim 1.7$  GPa. The FM2-paramagnetic curve appears just below 30 K and about 1.4 GPa, and goes away at a critical pressure  $P_{c3} \sim 2.7 - 2.8$  GPa. Superconductivity is found in the narrow pressure range 2.55-2.75 GPa below  $T_c = 0.14$  K.

The magnetic properties of this compound are governed by a saturation moment along the easy axis  $[10\bar{1}]$ , as indicated by the magnetization curve of a single crystal at 2 K shown in Fig. 31(a) [108]. The ordered magnetic moment goes from  $0.5\mu_B/U$  at ambient pressure in the ferromagnetic phase FM1 to  $0.07\mu_B/U$  at 2.4 GPa in the ferromagnetic phase FM2 [96]. The anisotropy of the magnetization remains at high temperatures, as can be seen in Fig. 31(b). The susceptibility data follow a Curie-Weiss law in the high-temperature paramagnetic region, with an effective magnetic moment around  $3.57 \mu_B/U$  that is pretty close to the  $5f^2$  free-ion value  $3.58 \mu_B/U$ . The small value of the ordered moment  $0.5\mu_B/U$  has been taken as evidence for the itinerant character of the  $5f$  electrons in the ferromagnetic phase, though such a low value could also be due to crystal-field effects [106, 109].

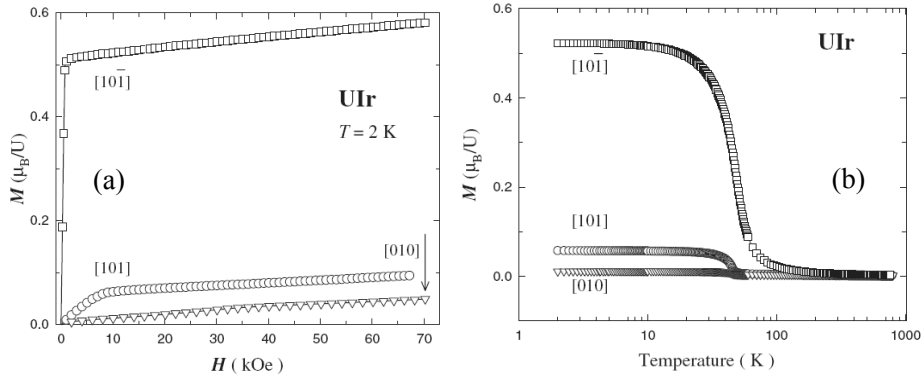


**Fig. 31** Magnetization as a function of (a) field strength at 2 K and (b) temperature in 10 kOe in a single crystal of UIr [108].

### 3.2.2 Electronic States

Quantum-oscillation and resistivity measurements provide evidence that the low-temperature metallic state of UIr is a Fermi liquid at ambient pressure. The dHvA measurements suggest that the Fermi surface of UIr is two-dimensional and consists mainly of nearly cylindrical sheets [97]. It has an effective mass  $m^* \sim 10 - 30 m_0$  and a mean free path  $l \sim 1270 \text{ \AA}$ . Such a value of the effective mass of the  $5f$  electrons leads to the classification of UIr as a moderate heavy-fermion compound.

Since the linear coefficient of the heat capacity  $\gamma_n \propto m^*$ , summing for all the branches yields the electronic specific-heat coefficient of 40-49 mJ/K<sup>2</sup>mol [97, 110]. There are no band-structure calculations for this compound.

Figure 32(a) shows the variation of the electrical resistivity of UIr as a function of pressure [105, 110]. At low pressure, in the ferromagnetic phase FM1, the resistivity follows  $\rho = \rho_0 + AT^n$ , with  $n \sim 2$  suggesting Fermi-liquid behavior. However, as pressure increases the behavior becomes non-Fermi-liquid like and eventually superconductivity appears in this regime. Figures 32(c-e) show the variation in  $n$ ,  $A$  and  $\rho_0$  as pressure increases. The non-Fermi-liquid behavior above  $\sim 1$  GPa may be related to critical fluctuations near the different magnetic transitions.

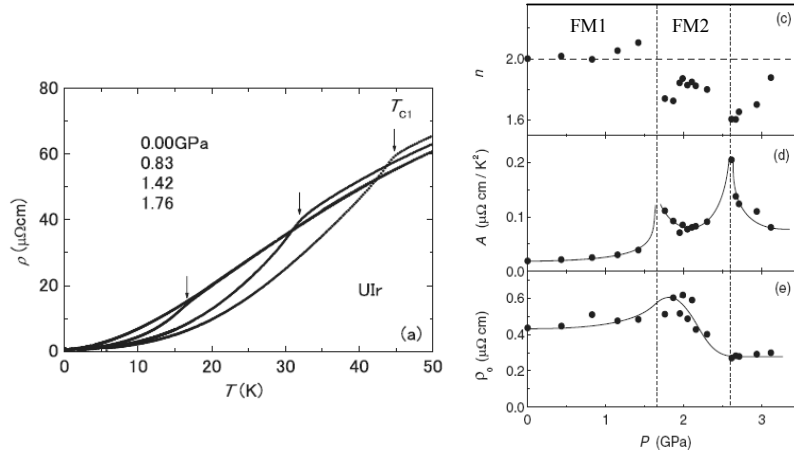


**Fig. 32** (a) Resistivity as a function of temperature of UIr at different pressures, and (c-e) variations in the parameters  $n$ ,  $A$  and  $\rho_0$  of  $\rho = \rho_0 + AT^n$  as pressure increases [108].

### 3.3 Superconducting State

Because of its extremely low critical temperature  $T_c = 0.14$  K (in most figures in this section this critical temperature is called  $T_{sc}$ ), there is little information on the superconducting state of UIr. Superconductivity seems to occur inside and near the quantum critical point of the FM2 phase, in the very narrow pressure range of 2.6-2.75 GPa [96]. In the ferromagnet UGe<sub>2</sub> with inversion symmetry the superconducting phase exists inside the ferromagnetic phase as well. Figure 33(a) shows the temperature dependence of the resistivity below 10 K and at 2.61 GPa, where it follows a non-Fermi-liquid form  $T^{1.6}$  [105]. Figure 33(b) is a close-up of the low-temperature region of the phase diagram where superconductivity appears (in this figure, FM3 denotes the ferromagnetic phase FM2).

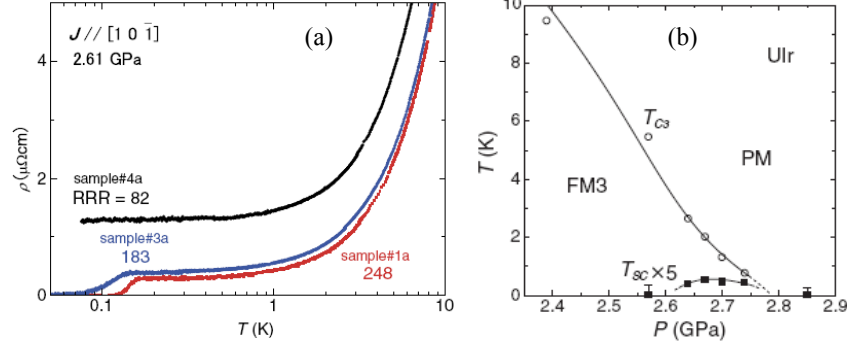


**Fig. 33** (a) Resistivity below 10 K and at 2.61 GPa of UIr showing a non-Fermi-liquid behavior. The three samples possess different RRR-values: 82, 183 and 248. (b) Low-temperature region of the phase diagram of UIr [107].

Up to now experimental indications of the existence of a superconducting phase in UIr come from measurements of resistivity in samples of different qualities. No definite diamagnetic signal has yet been observed in UIr (Fig. 34) [107]. The temperature dependence of the resistivity for three different samples is shown in Fig. 33(a). The data indicate that superconductivity becomes weaker as the residual resistivity ratio (RRR) of the samples drops. Such a strong suppression of  $T_c$  with increasing impurities/defects is typical of unconventional parity-conserving superconductors [27]. Recent theoretical works [111, 112] considered impurity effects on the critical temperature of superconductors without inversion symmetry. It was found that impurity scattering leads to a functional form of  $T_c$  that, up to a prefactor, is the same as the one for unconventional superconductor with inversion symmetry:  $\ln(T_c/T_{c0}) = \alpha \left[ \Psi\left(\frac{1}{2}\right) - \Psi\left(\frac{1}{2} - \frac{\Gamma}{2\pi T_c}\right) \right]$ . The suppression of  $T_c$  by impurities in non-centrosymmetric UIr agrees with this prediction [111, 112].

The upper critical field  $H_{c2}(T)$  in the direction of the easy axis  $[10\bar{1}]$  in the high-temperature region was determined by resistivity measurements in a sample with a very high RRR (Fig. 35) [105].  $T_c$  was defined as the midpoint of the resistivity drop. By assuming the standard empirical expression  $H_{c2}(T) = H_{c2}(0) [1 - (T/T_c)^2]$ , the zero-temperature upper critical field  $H_{c2}(0)$  was estimated as 26 mT corresponding to a coherence length of  $\xi(0) = 1100 \text{ \AA}$ . Since this value of  $H_{c2}(0)$  is smaller than the paramagnetic limiting field  $H_p = 280 \text{ mT}$  orbital depairing is the likely mechanism for the upper critical field in UIr.

It is believed that near a ferromagnetic quantum critical point spin fluctuations lead to Cooper pairing in a spin-triplet channel. There are some possible scenarios for the unexpected realization of superconductivity in this compound. It needs to be confirmed that FM2 is indeed a ferromagnetic phase, and not a canted antiferromagnetic phase that could yield pairing in the spin-single channel. A canted antiferromagnetic phase may be caused by the spin-orbit coupling and the low symmetry of the crystalline structure without inversion symmetry, as discussed by Dzyaloshinsky and Moriya. In this sense, it is important to note that the saturated mo-



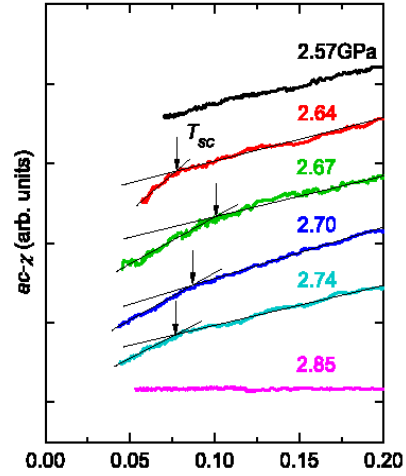


**Fig. 34** Temperature dependence of the ac susceptibility of UIr below 0.2 K at different pressure. Arrows indicate the onset temperatures [107].

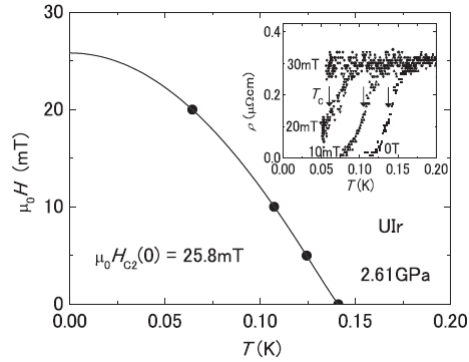


**Fig. 35** Upper critical field  $H_{c2}(T)$  along the easy axis [101] in UIr. The critical temperatures were defined by the midpoints of the resistivity drops in the inset [105].

ment of  $0.07 \mu_B/U$  in the FM2 phase is quite small. Another possibility is the FFLO state, in which at zero magnetic field electrons with momenta  $\mathbf{k}$  and  $-\mathbf{k}+\mathbf{q}$  can pair with nonzero angular momenta. A mean-field model has been recently proposed for superconductivity in non-centrosymmetric ferromagnets [113], in which the anti-symmetric spin-orbit coupling (ASOC) turns out to enhance both superconductivity and ferromagnetism in all spin channels. Future experiments will be absolutely important for the understanding of this unique superconductor.

#### 4 Comparison of the Superconducting States of CePt<sub>3</sub>Si, CeRhSi<sub>3</sub>, CeIrSi<sub>3</sub>, CeCoGe<sub>3</sub>, CeIrGe<sub>3</sub> and UIr

The superconducting properties of the non-centrosymmetric HF compounds have not been easy to determine. On the one hand, the CeTX<sub>3</sub> and UIr compounds only

superconduct under pressure, making technically difficult to study them. On the other hand, CePt<sub>3</sub>Si does become superconducting at ambient pressure, but has drawbacks in the crystal quality available. In spite of this, it has been possible to establish some of the characteristics of these materials.

The CeTX<sub>3</sub> materials, with tetragonal space group *I4mm*, and CePt<sub>3</sub>Si, with tetragonal space group *P4mm*, have the same generating point group *C<sub>4v</sub>* which lacks a mirror plane and a two-fold axis normal to the *c* axis. Thus, a Rashba-type interaction appears in all these compounds due to the missing of inversion symmetry. In contrast, UIr has a monoclinic lattice.

The Sommerfeld coefficient is much larger in CePt<sub>3</sub>Si than in CeTX<sub>3</sub> and UIr. Electron correlations should hence be stronger in CePt<sub>3</sub>Si. On the other hand, all compounds turn from Fermi-liquid to non-Fermi-liquid states as pressure is increased and become superconducting in the Fermi-liquid state, with the exception of UIr.

The behavior of the upper critical field  $H_{c2}$  in the CeTX<sub>3</sub> systems is very different from that in CePt<sub>3</sub>Si. In CeTX<sub>3</sub>,  $H_{c2\parallel c} > 22$  T and  $(-dH_{c2\parallel c}(T)/dT)_{T_c} > 17$  T/K are larger than  $H_{c2\parallel c} \approx 3$  T and  $(-dH_{c2\parallel c}(T)/dT)_{T_c} \sim 6.3$  T/K in CePt<sub>3</sub>Si. Moreover, in CeTX<sub>3</sub>  $H_{c2}(T)$  has a positive curvature, unlike in CePt<sub>3</sub>Si. In CeIrSi<sub>3</sub>, for example, superconductivity is anisotropic ( $H_{c2\parallel c}/H_{c2\parallel ab} > 3$ ), whereas in CePt<sub>3</sub>Si it is almost isotropic. There are clear signatures for unconventional superconductivity in CeIrSi<sub>3</sub>, CeRhSi<sub>3</sub> and CePt<sub>3</sub>Si, including evidence for line nodes in some cases. The fact that these compounds also support strong magnetic features and order suggests strongly that unconventional pairing mechanisms could be at work here. In this context it is particularly intriguing to analyze the role the antisymmetric spin-orbit coupling.

**Acknowledgements** We are grateful to M. Sigrist, S. Fujimoto, Y. Tada, D. F. Agterberg, K. Samokhin, F. Honda, Y. Matsuda, T. Sugawara, T. Terashima, H. Aoki, F. Lévy and I. Sheikin for helpful discussions. The work of N.K. was supported by KAKENHI (grant numbers 18684018 and 20102002) and partially by MEXT of Japan through Tohoku University GCOE program “Weaving Science Web beyond Particle-matter Hierarchy”. I.B. acknowledges initial support by the Venezuelan FONACIT (grant number S1-2001000693).

## References

1. E. Bauer, G. Hilscher, H. Michor, C. Paul, E.W. Scheidt, A. Griбанov, Y. Seropegin, H. Noel, M. Sigrist, P. Rogl, Phys. Rev. Lett. **92**, 027003 (2004)
2. A. Amato, E. Bauer, C. Baines, Phys. Rev. B **71**, 092501 (2005)
3. N. Metoki, K. Kaneko, T.D. Matsuda, A. Galatanu, T. Takeuchi, S. Hashimoto, T. Ueda, R. Settai, Y. Ōnuki, N. Bernhoeft, J. Phys.: Conf. Ser. **16**, L207 (2004)
4. E. Bauer, I. Bonalde, M. Sigrist, Low Temp. Phys. **31**, 748 (2005)
5. E. Bauer, H. Kaldarar, A. Prokofiev, E. Royanian, A. Amato, J. Sereni, W. Brämer-Escamilla, I. Bonalde, J. Phys. Soc. Jpn. **76**, 051009 (2007)
6. A. Griбанov, Y.D. Seropegin, A.I. Tursina, O.I. Bodak, P. Rogl, H. Noel, J. Alloys Compd. **383**, 286 (2004)
7. J.S. Kim, D.J. Mixson, D.J. Burnette, G.R. Stewart, J. Low. Temp. Phys. **147**, 135 (2007)

8. N. Tateiwa, Y. Haga, T.D. Matsuda, S. Ikeda, T. Yasuda, T. Takeuchi, R. Settai, Y. Ōnuki, J. Phys. Soc. Jpn. **74**, 1903 (2005)
9. S. Hashimoto, T. Yasuda, T. Kubo, H. Shishido, T. Ueda, R. Settai, T.D. Matsuda, Y. Haga, H. Harima, Y. Ōnuki, J. Phys.: Condens. Matter **16**, L287 (2004)
10. T. Yasuda, H. Shishido, T. Ueda, S. Hashimoto, R. Settai, T. Takeuchi, T.D. Matsuda, Y. Haga, Y. Ōnuki, J. Phys. Soc. Jpn. **73**, 1657 (2004)
11. G. Motoyama, K. Maeda, Y. Oda, J. Phys. Soc. Jpn. **77**, 044710 (2008)
12. H. Mukuda, S. Nishide, A. Harada, K. Iwasaki, M. Yogi, M. Yashima, Y. Kitaoka, M. Tsujino, T. Takeuchi, R. Settai, Y. Ōnuki, E. Bauer, K.M. Itoh, E.E. Haller, J. Phys. Soc. Jpn. **78**, 014705 (2009)
13. I. Bonalde, R.L. Ribeiro, W. Brämer-Escamilla, C. Rojas, E. Bauer, A. Prokofiev, Y. Haga, T. Yasuda, Y. Ōnuki, New J. Phys. **11**, 055054 (2009)
14. R.L. Ribeiro, I. Bonalde, Y. Haga, R. Settai, Y. Ōnuki, J. Phys. Soc. Jpn. **78**, 115002 (2009)
15. K.V. Samokhin, E.S. Zijlstra, S.K. Bose, Phys. Rev. B **69**, 094514 (2004)
16. I.A. Sergienko, S.H. Curnoe, Phys. Rev. B **70**, 214510 (2004)
17. P.A. Frigeri, D.F. Agterberg, A. Koga, M. Sigrist, Phys. Rev. Lett. **92**, 097001 (2004)
18. S. Fujimoto, J. Phys. Soc. Jpn. **76**, 051008 (2007)
19. Y. Yanase, M. Sigrist, J. Phys. Soc. Jpn. **76**, 043712 (2007)
20. M. Yogi, H. Mukuda, Y. Kitaoka, S. Hashimoto, T. Yasuda, R. Settai, T.D. Matsuda, Y. Haga, Y. Ōnuki, P. Rogl, E. Bauer, J. Phys. Soc. Jpn. **75**, 013709 (2006)
21. P.A. Frigeri, D.F. Agterberg, M. Sigrist, New J. Phys. **6**, 115 (2004)
22. K.V. Samokhin, Phys. Rev. Lett. **94**, 027004 (2005)
23. R.P. Kaur, D.F. Agterberg, M. Sigrist, Phys. Rev. Lett. **94**, 137002 (2005)
24. K. V. Samokhin, Phys. Rev. B **78**, 224520 (2008)
25. E. Helfand, N.R. Werthamer, Phys. Rev. **147**, 288 (1966)
26. I. Bonalde, W. Brämer-Escamilla, E. Bauer, Phys. Rev. Lett. **94**, 207002 (2005)
27. V.P. Mineev, K.V. Samokhin, *Introduction to unconventional superconductivity* (Gordon and Breach Science Publishers, Amsterdam, 1999)
28. I. Bonalde, W. Brämer-Escamilla, Y. Haga, E. Bauer, Y. Yasuda, Y. Ōnuki, Physica C **460**, 659 (2007)
29. K. Izawa, Y. Kasahara, Y. Matsuda, K. Behnia, T. Yasuda, R. Settai, Y. Ōnuki, Phys. Rev. Lett. **94**, 197002 (2005)
30. T. Takeuchi, T. Yasuda, M. Tsujino, H. Shishido, R. Settai, H. Harima, Y. Ōnuki, J. Phys. Soc. Jpn. **76**, 014702 (2007)
31. C. Kübert, P.J. Hirschfeld, Phys. Rev. Lett. **80**, 4963 (1998)
32. P. Lejay, I. Higashi, B. Chevalier, J. Etourneau, P. Hagenmuller, Mater. Res. Bull. **19**, 115 (1984)
33. F. Steglich, J. Aarts, C.D. Bredl, W. Lieke, D. Meschede, W. Franz, H. Schäfer, Phys. Rev. Lett. **43**, 1892 (1979)
34. D. Jaccard, K. Behnia, J. Sierro, Phys. Lett. A **163**, 475 (1992)
35. N.D. Mathur, F.M. Grosche, S.R. Julian, I.R. Walker, D.M. Freye, R.K.W. Haselwimmer, G.G. Lonzarich, Nature **394**, 39 (1998)
36. R. Movshovich, T. Graf, D. Mandrus, J.D. Thompson, J.L. Smith, Z. Fisk, Phys. Rev. B **53**, 8241 (1996)
37. T.T.M. Palstra, A.A. Menovsky, J. Vandenberg, A.J. Dirkmaat, P.H. Kes, G.J. Nieuwenhuys, J.A. Mydosh, Phys. Rev. Lett. **55**, 2727 (1985)
38. A. Szytula, in *Handbook of Magnetic Materials*, vol. 6, ed. by K.H.J. Buschow (Elsevier Science Publishers B. V., Amsterdam, Tokyo, North-Holland, 1991), p. 152
39. N. Kimura, K. Ito, K. Saitoh, Y. Umeda, H. Aoki, T. Terashima, Phys. Rev. Lett. **95**, 247004 (2005)
40. I. Sugitani, Y. Okuda, H. Shishido, T. Yamada, A. Thamzavel, E. Yamamoto, T.D. Matsuda, Y. Haga, T. Takeuchi, R. Settai, Y. Ōnuki, J. Phys. Soc. Jpn. **75**, 043703 (2006)
41. R. Settai, I. Sugitani, Y. Okuda, A. Thamzavel, M. Nakashima, Y. Ōnuki, H. Harima, J. Magn. Magn. Mater. **310**, 844 (2007)

42. F. Honda, I. Bonalde, K. Shimizu, S. Yoshiuchi, Y. Hirose, T. Nakamura, R. Settai, Y. Ōnuki, *Phys. Rev. B* **81**, 140507 (2010)
43. T. Kawai, H. Muranaka, M.A. Measson, T. Shimoda, Y. Doi, T.D. Matsuda, Y. Haga, G. Knebel, G. Lapertot, D. Aoki, J. Flouquet, T. Takeuchi, R. Settai, Y. Ōnuki, *J. Phys. Soc. Jpn.* **77**, 064716 (2008)
44. A. Thamizhavel, T. Takeuchi, T.D. Matsuda, Y. Haga, K. Sugiyama, R. Settai, Y. Ōnuki, *J. Phys. Soc. Jpn.* **74**, 1858 (2005)
45. S. Mock, C. Pfeleiderer, H. von Löhneysen, *J. Low. Temp. Phys.* **115**, 1 (1999)
46. S. Paschen, E. Felder, H.R. Ott, *Europ. Phys. J. B* **2**, 169 (1998)
47. S.A.M. Mentink, N.M. Bos, B.J. Vanrossum, G.J. Nieuwenhuys, J.A. Mydosh, K.H.J. Buschow, *J. Appl. Phys.* **73**, 6625 (1993)
48. M. Kontani, H. Ido, H. Ando, T. Nishioka, Y. Yamaguchi, *J. Phys. Soc. Jpn.* **63**, 1652 (1994)
49. H. Sugawara, S.R. Saha, T.D. Matsuda, Y. Aoki, H. Sato, J.L. Gavilano, H.R. Ott, *Physica B* **261**, 16 (1999)
50. M. Nakashima, K. Tabata, A. Thamizhavel, T.C. Kobayashi, M. Hedo, Y. Uwatoko, K. Shimizu, R. Settai, Y. Ōnuki, *J. Phys.: Condens. Matter* **16**, L255 (2004)
51. A.V. Morozkin, Y.D. Seropegin, *J. Alloys Compd.* **237**, 124 (1996)
52. K. Ghosh, S. Ramakrishnan, S.K. Dhar, S.K. Malik, G. Chandra, V.K. Pecharsky, K.A. Gschneidner, Z. Hu, W.B. Yelon, *Phys. Rev. B* **52**, 7267 (1995)
53. T. Takabatake, Y. Maeda, H. Fujii, S. Ikeda, S. Nishigori, T. Fujita, A. Minami, I. Oguro, K. Sugiyama, K. Oda, M. Date, *Physica B* **188**, 734 (1993)
54. R. Settai, Y. Miyauchi, T. Takeuchi, F. Lévy, I. Sheikin, Y. Ōnuki, *J. Phys. Soc. Jpn.* **77**, 073705 (2008)
55. Y. Muro, Ph.D. thesis, The University of Tokio (2000)
56. V.K. Pecharsky, O.B. Hyun, K.A. Gschneidner, *Phys. Rev. B* **47**, 11839 (1993)
57. A. Das, R.K. Kremer, R. Pöttgen, B. Ouladdiaf, *Physica B* **378-80**, 837 (2006)
58. B. Rupp, P. Rogl, F. Hulliger, *J. Less-Common Met.* **135**, 113 (1987)
59. D. Eom, M. Ishikawa, J. Kitagawa, N. Takeda, *J. Phys. Soc. Jpn.* **67**, 2495 (1998)
60. Y. Muro, D. Eom, N. Takeda, M. Ishikawa, *J. Phys. Soc. Jpn.* **67**, 3601 (1998)
61. T. Kawai, M. Nakashima, Y. Okuda, H. Shishido, T. Shimoda, T.D. Matsuda, Y. Haga, T. Takeuchi, M. Hedo, Y. Uwatoko, R. Settai, Y. Ōnuki, *J. Phys. Soc. Jpn. Suppl. A* **76**, 166 (2007)
62. J. Kitagawa, Y. Muro, N. Takeda, M. Ishikawa, *J. Phys. Soc. Jpn.* **66**, 2163 (1997)
63. P. Haen, P. Lejay, B. Chevalier, B. Lloret, J. Etourneau, M. Sera, *J. Less-Common Met.* **110**, 321 (1985)
64. T. Kawai, Y. Okuda, H. Shishido, A. Thamizhavel, T.D. Matsuda, Y. Haga, M. Nakashima, T. Takeuchi, M. Hedo, Y. Uwatoko, R. Settai, Y. Ōnuki, *J. Phys. Soc. Jpn.* **76**, 014710 (2007)
65. H. Yamamoto, M. Ishikawa, K. Hasegawa, J. Sakurai, *Phys. Rev. B* **52**, 10136 (1995)
66. T. Kawai, Split fermi surface properties and superconductivity in the non-centrosymmetric crystal structure. Ph.D. thesis, Osaka University (2008)
67. Y. Muro, M. Ishikawa, K. Hirota, Z. Hiroi, N. Takeda, N. Kimura, H. Aoki, *J. Phys. Soc. Jpn.* **76**, 033706 (2007)
68. Y. Okuda, Y. Miyauchi, Y. Ida, Y. Takeda, C. Tonohiro, Y. Oduchi, T. Yamada, N.D. Dung, T.D. Matsuda, Y. Haga, T. Takeuchi, M. Hagiwara, K. Kindo, H. Harima, K. Sugiyama, R. Settai, Y. Ōnuki, *J. Phys. Soc. Jpn.* **76**, 044708 (2007)
69. N. Aso, H. Miyano, H. Yoshizawa, N. Kimura, T. Komatsubara, H. Aoki, *J. Magn. Magn. Mater.* **310**, 602 (2007)
70. H. Miyano, Spin correlation in pressure-induced superconductors. Master's Thesis, The University of Tokyo (2007)
71. F. Tomioka, I. Umehara, T. Ono, M. Hedo, Y. Uwatoko, N. Kimura, *Jpn. J. Appl. Phys.* **46**, 3090 (2007)
72. N. Kimura, Y. Muro, H. Aoki, *J. Phys. Soc. Jpn.* **76**, 051010 (2007)
73. K. Kadowaki, S.B. Woods, *Sol. State Commun.* **58**, 507 (1986)
74. K. Kaneko, N. Metoki, T. Takeuchi, T.D. Matsuda, Y. Haga, A. Thamizhavel, R. Settai, Y. Ōnuki, *J. Phys.: Conf. Ser.* **150**, 042082 (2009)

75. N. Tateiwa, Y. Haga, T.D. Matsuda, S. Ikeda, E. Yamamoto, Y. Okuda, Y. Miyauchi, R. Settai, Y. Ōnuki, *J. Phys. Soc. Jpn.* **76**, 083706 (2007)
76. R. Settai, Y. Okuda, I. Sugitani, Y. Ōnuki, T.D. Matsuda, Y. Haga, H. Harima, *Int. J. Mod. Phys. B* **21**, 3238 (2007)
77. G. Knebel, D. Aoki, G. Lapertot, B. Salce, J. Flouquet, T. Kawai, H. Muranaka, R. Settai, Y. Ōnuki, *J. Phys. Soc. Jpn.* **78**, 074714 (2009)
78. H. Mukuda, T. Fujii, T. Ohara, A. Harada, M. Yashima, Y. Kitaoka, Y. Okuda, R. Settai, Y. Ōnuki, *Phys. Rev. Lett.* **100**, 107003 (2008)
79. R.A. Fisher, F. Bouquet, N.E. Phillips, M.F. Hundley, P.G. Pagliuso, J.L. Sarrao, Z. Fisk, J.D. Thompson, *Phys. Rev. B* **65**, 224509 (2002)
80. S. Araki, M. Nakashima, R. Settai, T.C. Kobayashi, Y. Ōnuki, *J. Phys.: Condens. Matter* **14**, L377 (2002)
81. G. Knebel, D. Braithwaite, P.C. Canfield, G. Lapertot, J. Flouquet, *Phys. Rev. B* **65**, 024425 (2002)
82. K. Miyake, H. Maebashi, *J. Phys. Soc. Jpn.* **71**, 1007 (2002)
83. F. Lévy, I. Sheikin, B. Grenier, A.D. Huxley, *Science* **309**, 1343 (2005)
84. S. Uji, H. Shinagawa, T. Terashima, T. Yakabe, Y. Terai, M. Tokumoto, A. Kobayashi, H. Tanaka, H. Kobayashi, *Nature* **410**, 908 (2001)
85. R.R. Hake, *Appl. Phys. Lett.* **10**, 189 (1967)
86. L.N. Bulaevskii, O.V. Dolgov, M.O. Pfitsyn, *Phys. Rev. B* **38**, 11290 (1988)
87. A. Huxley, I. Sheikin, E. Ressouche, N. Kernavanois, D. Braithwaite, R. Calemczuk, J. Flouquet, *Phys. Rev. B* **63**, 144519 (2001)
88. I. Sheikin, A. Huxley, D. Braithwaite, J.P. Brison, S. Watanabe, K. Miyake, J. Flouquet, *Phys. Rev. B* **64**, 220503 (2001)
89. T. Terashima, Y. Takahide, T. Matsumoto, S. Uji, N. Kimura, H. Aoki, H. Harima, *Phys. Rev. B* **76**, 054506 (2007)
90. Y. Tada, N. Kawakami, S. Fujimoto, *Phys. Rev. Lett.* **101**, 267006 (2008)
91. D.F. Agterberg, P.A. Frigeri, R.P. Kaur, A. Koga, M. Sigrist, *Physica B* **378-80**, 351 (2006)
92. D.F. Agterberg, R.P. Kaur, *Phys. Rev. B* **75**, 064511 (2007)
93. N. Kimura, K. Ito, H. Aoki, S. Uji, T. Terashima, *Phys. Rev. Lett.* **98**, 197001 (2007)
94. Y. Tada, N. Kawakami, S. Fujimoto, *J. Phys. Soc. Jpn.* **77**, 054707 (2008)
95. A. Dommann, F. Hulliger, T. Siegrist, P. Fischer, *J. Magn. Magn. Mater.* **67**, 323 (1987)
96. T. Akazawa, H. Hidaka, T. Fujiwara, T.C. Kobayashi, E. Yamamoto, Y. Haga, R. Settai, Y. Ōnuki, *J. Phys.: Condens. Matter* **16**, L29 (2004)
97. E. Yamamoto, Y. Haga, H. Shishido, H. Nakawaki, Y. Inada, R. Settai, Y. Ōnuki, *Physica B* **312**, 302 (2002)
98. P.W. Anderson, *J. Phys. Chem. Solids* **11**, 26 (1959)
99. P.W. Anderson, *Phys. Rev. B* **30**, 4000 (1984)
100. S.S. Saxena, P. Agarwal, K. Ahilan, F.M. Grosche, R.K.W. Haselwimmer, M.J. Steiner, E. Pugh, I.R. Walker, S.R. Julian, P. Monthoux, G.G. Lonzarich, A. Huxley, I. Sheikin, D. Braithwaite, J. Flouquet, *Nature* **406**, 587 (2000)
101. D. Aoki, A. Huxley, E. Ressouche, D. Braithwaite, J. Flouquet, J.P. Brison, E. Lhotel, C. Paulsen, *Nature* **413**, 613 (2001)
102. Y. Ōnuki, R. Settai, K. Sugiyama, Y. Inada, T. Takeuchi, Y. Haga, E. Yamamoto, H. Harima, H. Yamagami, *J. Phys.: Condens. Matter* **19**, 125203 (2007)
103. T.C. Kobayashi, H. Hidaka, T. Fujiwara, M. Tanaka, K. Takeda, T. Akazawa, K. Shimizu, S. Kirita, R. Asai, H. Nakawaki, M. Nakashima, R. Settai, E. Yamamoto, Y. Haga, Y. Ōnuki, *J. Phys.: Condens. Matter* **19**, 125205 (2007)
104. E. Yamamoto, Y. Haga, S. Ikeda, T.D. Matsuda, T. Akazawa, H. Kotegawa, T.C. Kobayashi, Y. Ōnuki, *J. Magn. Magn. Mater.* **310**, e123 (2007)
105. T. Akazawa, H. Hidaka, H. Kotegawa, T.C. Kobayashi, T. Fujiwara, E. Yamamoto, Y. Haga, R. Settai, Y. Ōnuki, *J. Phys. Soc. Jpn.* **73**, 3129 (2004)
106. S. Sakarya, N.H. van Dijk, A. de Visser, E. Bruck, Y. Huang, J. Perenboom, H. Rakoto, J.M. Broto, *J. Magn. Magn. Mater.* **310**, 1564 (2007)

107. T.C. Kobayashi, A. Hori, S. Fukushima, H. Hidaka, H. Kotegawa, T. Akazawa, K. Takeda, Y. Ohishi, E. Yamamoto, *J. Phys. Soc. Jpn.* **76**, 051007 (2007)
108. A. Galatanu, Y. Haga, E. Yamamoto, T.D. Matsuda, S. Ikeda, Y. Ōnuki, *J. Phys. Soc. Jpn.* **73**, 766 (2004)
109. A. Galatanu, Y. Haga, T.D. Matsuda, S. Ikeda, E. Yamamoto, D. Aoki, T. Takeuchi, Y. Ōnuki, *J. Phys. Soc. Jpn.* **74**, 1582 (2005)
110. E.D. Bauer, E.J. Freeman, C. Sirvent, M.B. Maple, *J. Phys.: Condens. Matter* **13**, 5675 (2001)
111. P.A. Frigeri, D.F. Agterberg, I. Milat, M. Sigrist, *Europ. Phys. J. B* **54**, 435 (2006)
112. V.P. Mineev, K.V. Samokhin, *Phys. Rev. B* **75**, 184529 (2007)
113. J. Linder, A.H. Nevidomskyy, A. Sudbo, *Phys. Rev. B* **78**, 172502 (2008)